The ELAIS deep X-ray survey - I. Chandra source catalogue and first results

Article (Published Version)

Mon. Not. R. Astron. Soc. **343,** 293–305 (2003)

The ELAIS deep X-ray survey – I. *Chandra* source catalogue and first results

J. C. Manners,[1⋆†] O. Johnson,[1] O. Almaini,[1] C. J. Willott,[2] E. Gonzalez-Solares,[3] A. Lawrence,[1] R. G. Mann,[1] I. Perez-Fournon,[4] J. S. Dunlop,[1] R. G. McMahon,[5] S. J. Oliver,[3] M. Rowan-Robinson[6] and S. Serjeant[7]

[1]*Institute for Astronomy, University of Edinburgh, Royal Observatory, Blackford Hill, Edinburgh EH9 3HJ*
[2]*Astrophysics, Department of Physics, Keble Rd, Oxford OX1 3RH*
[3]*Astronomy Centre, CPES, University of Sussex, Falmer, Brighton, BN1 9QJ*
[4]*Instituto de Astrofisica de Canarias, 38200 La Laguna, Tenerife, Spain*
[5]*Institute of Astronomy, Madingley Road, Cambridge, CB3 0HA*
[6]*Astrophysics Group, Blackett Laboratory, Imperial College, Prince Consort Rd, London SW7 2BW*
[7]*Unit for Space Sciences and Astrophysics, School of Physical Sciences, University of Kent, Canterbury CT2 7NZ*

Accepted 2003 March 28. Received 2003 March 27; in original form 2002 July 26

ABSTRACT

We present an analysis of two deep (75 ks) *Chandra* observations of the European Large Area *Infrared Space Observatory* (*ISO*) Survey (ELAIS) fields N1 and N2 as the first results from the ELAIS deep X-ray survey. This survey is being conducted in well-studied regions with extensive multiwavelength coverage. Here we present the *Chandra* source catalogues along with an analysis of source counts, hardness ratios and optical classifications. A total of 233 X-ray point sources are detected in addition to two soft extended sources, which are found to be associated with galaxy clusters. An overdensity of sources is found in N1 with 30 per cent more sources than N2, which we attribute to large-scale structure. A similar variance is seen between other deep *Chandra* surveys. The source count statistics reveal an increasing fraction of hard sources at fainter fluxes. The number of galaxy-like counterparts also increases dramatically towards fainter fluxes, consistent with the emergence of a large population of obscured sources.

Key words: catalogues – surveys – galaxies: active – X-rays: diffuse background – X-rays: galaxies – X-rays: general.

1 INTRODUCTION

The results of recent deep X-ray surveys reveal that almost the entire X-ray background can be resolved into discrete sources. The *ROSAT* Deep Survey (Hasinger et al. 1998) resolved 70–80 per cent of the 0.5–2 keV background at a flux level of 1×10^{-15} erg s^{-1} cm^{-2}. Observations with *Chandra* and *XMM-Newton* are now pushing the detection limits even further. In particular, the unprecedented resolution of *Chandra* allows extremely deep observations that are not limited by source confusion. This has been exploited in the *Chandra* Deep Field North (CDFN; Brandt et al. 2001) and the *Chandra* Deep Field South (CDFS; Giacconi et al. 2002). In the CDFN, 2 Ms of data have been accumulated reaching a flux limit of $\sim 1.5 \times 10^{-17}$ erg s^{-1} cm^{-2} in the 0.5–2 keV band (Barger et al. 2003). However, the greatest advances have been at higher energies where *Chandra* is now beginning to resolve the 2–8 keV background.

The majority of sources resolved by *ROSAT* were found to have spectra that were too steep to account for the flat spectrum of the hard X-ray background. However, towards fainter fluxes a new population emerged in the *ROSAT* data with intrinsically harder X-ray spectra (Hasinger et al. 1993; Almaini et al. 1996). *Chandra* is now uncovering a large number of hard spectrum sources, and the majority of the 2–8 keV background has been resolved. Over the flux range 2×10^{-16} to 10^{-13} erg s^{-1} cm^{-2} the contribution of resolved sources to the 2–8 keV background is 1.1×10^{-11} erg s^{-1} cm^{-2} deg^{-2} (Cowie et al. 2002). This translates to ∼65–85 per cent of the background as measured by Vecchi et al. (1999 *Beppo*-Sax) and Ueda et al. (1999 *ASCA*).

Early spectroscopic observations are finding a majority of the sources with hard X-ray spectra to be Type II active galactic nuclei (AGN), indicated by the presence of narrow lines (Tozzi et al. 2001; Barger et al. 2001a; Hornschemeier et al. 2001). Most of these are found at $z < 1$. However, a considerable fraction of the hard X-ray sources are optically faint, probably due to obscuration, and provide

⋆E-mail: manners@pd.astro.it
†Present address: Dipartimento di Astronomia, dell'Universita di Padova, Vicolo dell'Osservatorio, 2-35122 Padova, Italy.

challenging targets for spectroscopic identification. Sources identified as Type I AGN display softer X-ray spectra and are observed to have a higher median redshift.

There are still a number of unanswered questions relating to the properties of the hard X-ray populations at longer wavelengths. AGN with large X-ray absorbing columns do not always appear as Type II AGN in the optical (e.g. Maiolino et al. 2001; Willott et al. 2003). The relationship between gas and dust absorption in AGN remains unclear. It is also uncertain where the absorbed radiation may be re-radiated. Approximately ∼7 per cent of X-ray sources in the CDFN are submillimetre sources (Barger et al. 2001b), however it is unknown whether this is the result of reprocessed nuclear emission or due to a starburst component. Almaini et al. (2003) find evidence for a strong angular cross-correlation between the X-ray and submillimetre populations. They suggest that there may be an evolutionary sequence in these galaxies between the major episode of star formation (submillimetre sources) and the onset of quasar activity (X-ray sources). To more fully understand the nature of these sources will require in-depth multiwavelength studies of the X-ray source population.

We are conducting a deep X-ray survey with *Chandra* and *XMM* in two of the European Large Area *Infrared Space Observatory* (*ISO*) Survey (ELAIS) fields, N1 and N2. These high latitude fields were chosen for their low cirrus emission, and have a wealth of multiwavelength data available. Both fields have been observed with *ISO* at 7, 15, 90 and 175 μm (Oliver et al. 2000), with the Very Large Array (VLA) at 1.4 GHz (Ciliegi et al. 1999; Ivison et al. 2002), and have deep g', r', i', H and K imaging (Gonzalez-Solares et al., in preparation, hereafter Paper II). Region N2 has been mapped with the Submillimetre Common User Bolometer Array (SCUBA) to 8 mJy at 850 μm (Fox et al. 2002; Scott et al. 2002). As well as the *Chandra* observations described here, *XMM-Newton* observations in region N1 (5 × 30 ks pointings) are awaiting scheduling.

In this paper we present the analysis of the *Chandra* X-ray data and the *Chandra* source catalogue. Paper II will present details of the optical identifications.

2 THE X-RAY DATA

The ELAIS Deep X-ray Survey (EDXS) is being conducted in the northern ELAIS regions N1 and N2. The *Chandra* data consist of approximately 75 ks exposures in each field. Region N1 was observed on 2000 August 3–4 (OBS_ID 888) and N2 on 2000 August 2–3 (OBS_ID 887). The nominal aimpoints were: N1, 16:10:20.11 +54:33:22.3; and N2, 16:36:46.99 +41:01:33.7. The ACIS-I chips were used with the addition of ACIS-S2 and ACIS-S4.

Analysis was carried out on data reprocessed with version R4CU5UPD14.1 of the pipeline processing software. The data were reduced using the CIAO software package (version 2.1). Bad pixels and columns were removed and data were filtered to eliminate high background times. The latter was achieved through constructing a light curve for background regions and identifying periods of intense background activity due to solar flares. One obvious flaring period was identified over the course of the observations resulting in the removal of 1552 s from the data in region N1. More stringent conditions for the removal of high background times were not thought necessary, considering the low level of the quiescent background. After filtering, exposures in fields N1 and N2 were 71.5 and 73.4 ks, respectively.

Exposure maps were constructed to account for variations in effective exposure across an image. This incorporates the positions of bad pixels, dithering, and vignetting. The effective exposure is significantly affected by the energy of the source counts. To account for this, an assumed source spectrum is convolved with the quantum efficiency of the chip and the effective area of the mirrors. The resulting map provides an estimate of the effective exposure (cm^2 s) at each point on the image. For our images, we used a power-law model spectrum, with photon index $\Gamma = 1.7$.

3 SOURCE DETECTION

Sources were detected using a wavelet method, specifically the WAVDETECT program (Freeman et al. 2002) included with the CIAO software package. The 'Mexican Hat' wavelet function is used, which consists of a positive core similar to a canonical point spread function (PSF), surrounded by a negative annulus. The overall normalization is zero. The zero-crossing point is at a radius of $\sqrt{2}i$, and the minimum at $2i$, where i refers to the scale size in pixels. The correlation of this wavelet function with an image will reveal sources where correlation values are larger than a pre-defined threshold.

A 2 × 2 binned image was used, giving a pixel size of 0.984 arcsec. The threshold for source detection was set such that the probability of erroneously identifying a given pixel with a source is 9.5×10^{-7}. This translates to a mean detection of 1.0 false sources over the region of the four ACIS-I chips. Wavelet scales were chosen at $i = 2, 2\sqrt{2}, 4, 4\sqrt{2}, 8, 8\sqrt{2}, 16, 16\sqrt{2}$, and 32 pixels. The minimum scale was chosen to enclose ∼90 per cent encircled energy of an on-axis PSF. Larger scales can then match the increased size of off-axis and resolved sources. The algorithm also uses an exposure map to correct for inconsistencies across the chips.

Sources were detected in three bands: 0.5–8 keV (full band), 0.5–2 keV (soft band) and 2–8 keV (hard band). Below 0.5 keV the quantum efficiency (including the optical blocking filters) of the front illuminated chips drops off steeply. A steep rise is also observed in the background rate due to charged particles. Beyond 8 keV the effective area of the mirrors is sharply decreasing whilst the background rate is again beginning to rise.

In order to verify that no sources were missed, we also ran a source detection on the 0.3–10 keV band. All sources found were also detected in the 0.5–8 keV band and, overall, fewer sources were detected.

3.1 Sample reliability and detection efficiency

For the purposes of source detection, counts flagged as cosmic-ray afterglows were removed from the image. This procedure is known to also remove several percent of source photons. Therefore, to obtain reliable measurements of source flux and extent, a second run of the WAVDETECT algorithm was performed on an image where the flagged counts were reinstated. Only sources obtained in the original source detection were used.

WAVDETECT simulations (Freeman et al. 2002) suggest a mean of 1.0 false sources will be detected over the region of the four ACIS-I chips. We also impose a cut-off at a signal-to-noise ratio (S/N) of 3.0, principally for the purpose of defining a flux limit. This has the effect of removing a handful of the least significant sources, further improving the reliability of the sample.

The detection efficiency of WAVDETECT is yet to be definitively determined. Early simulations have been performed by V. Kashyap (private communication) to determine the probability of detecting sources of given strengths. In order to gain an indication of the number of sources missing from our list of detections, we have made crude extrapolations to these simulations. These indicate that

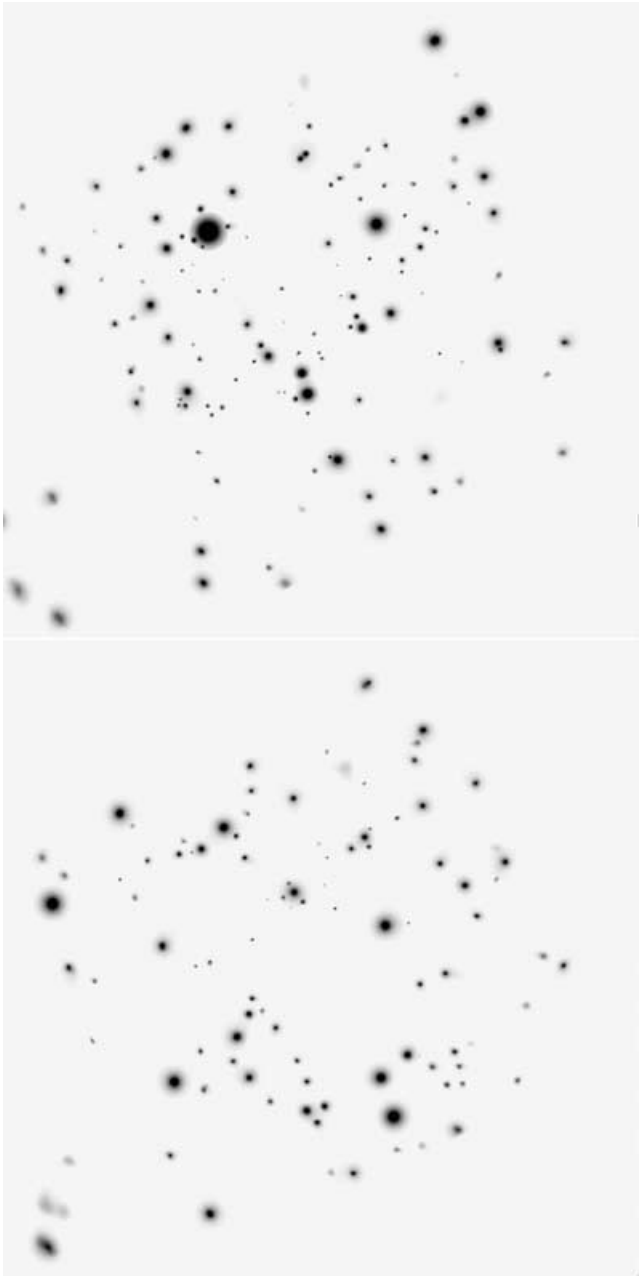

Figure 1. Full-band source images of the *Chandra* fields N1 (top) and N2 (bottom). This is a noise-free reconstruction of the raw data using the source properties and correlation images output from the source detection algorithm WAVDETECT. This figure can be seen in colour in the on-line version of the journal in *Synergy*, where the colours are constructed from the soft-band (red), full-band (green) and hard-band (blue).

we detect ∼98.5–99.5 per cent of the sources with intrinsic strengths above the S/N limit of our sample.

4 THE *CHANDRA* SOURCE CATALOGUE

A total of 233 X-ray sources have been detected in the two fields (Fig. 1). In N1 there are 127 sources in the full band (0.5–8 keV), 101 in the soft band (0.5–2 keV) including two extra sources not detected in the full band, and 72 sources in the hard band (2–8 keV) including one extra source not detected in the full band. There are 57 sources detected in both the soft and hard bands. In N2 there are 98 sources in the full band, 81 in the soft band (including three extra sources not in the full band), and 52 sources in the hard band (including two extra sources not in the full band). There are 41 sources detected in both the soft and hard bands.

The International Astronomical Union (IAU) name for the catalogued sources is CXOEN1 JHHMMSS.s+DDMMSS, for sources in N1 (Table 1), and CXOEN2 JHHMMSS.s+DDMMSS for sources in N2 (Table 2). Coordinates are truncated to the above accuracy.

Tables 1 and 2 display the full catalogue. Sources are detected to a S/N limit of 3, defined as

$$S/N = C/(1 + \sqrt{0.75 + B}) \quad (1)$$

where C are the net source counts, and B are the background counts within the 'source cell', a region defined by WAVDETECT assumed to contain effectively all of the source counts (Freeman et al. 2002). It should be noted that the source cell used here may be larger than regions used for conventional aperture photometry. The values calculated for S/N may therefore be lower than those expected from such methods. The denominator of equation (1) is an approximate expression for the error on the background counts (a small number statistic). This comes from Gehrels (1986, equation 7), which gives the upper confidence level equivalent to a 1σ Gaussian error. For sources that do not reach the S/N limit in a certain band, an upper flux limit has been calculated from equation (5) (Section 5, this paper).

Source coordinates have been astrometrically corrected using calibrated r'-band images (to a depth of $r' \sim 26$). High S/N *Chandra* sources were matched with stellar r'-band counterparts. 16 sources were used in N1 and 11 in N2, with a good spread across the fields. The Starlink package ASTROM was used to perform a six-parameter fit (zero points, scales in x and y, orientation and non-perpendicularity). The rms residuals were all less than 1 arcsec, randomly distributed with a mean of ∼0.4 arcsec. The positional error quoted in the catalogue is the error on the centroid position from the source detection algorithm, with 0.4 arcsec added in quadrature to represent astrometric error.

Net counts are quoted as the total source counts (background subtracted) in the full energy band (0.5–8 keV). Where sources are only detected in the soft or hard bands, the net counts represent counts in this band only.

Flux values are calculated assuming a power-law source spectrum of the form $F = \nu^{-\alpha}$ with $\alpha = 0.7$. The effective area will vary as a function of α depending on the response of the detector. If the slope of the spectrum is known for a given source, Fig. 2 can be used to calculate the true flux from the value given in the catalogue. This figure has been calculated by passing model spectra of slope α through the total response matrix of the detector. For illustrative purposes we use the response matrix at a position corresponding to the source N1_23 which lies 4.5 arcmin from the field centre.

5 SOURCE COUNTS

In this section we calculate the cumulative source counts, $N(>S)$, and the differential source counts, $n(S)$, in the three bands. We first outline details of the calculation (Section 5.1) which requires knowledge of the available area of the survey as a function of flux. In Section 5.2 we present our results and comparisons with other surveys, while in Section 5.3 we describe our source contribution to the hard X-ray background.

Table 1. *Chandra* sources in the ELAIS N1 field.

ID	CXOEN1	RA (J2000)	Dec. (J2000)	Err (arcsec)	Net counts	S/N	Flux ($\times 10^{-14}$ erg cm^{-2} s^{-1}) (0.5–8 keV)	(0.5–2 keV)	(2–8 keV)	HR
N1_1	J161121.8+543402	16:11:21.88	+54:34:02.7	0.65	76.3	17.4	1.24 ± 0.15	0.48 ± 0.07	<0.41	−0.32 ± 0.10
N1_2	J161113.1+543748	16:11:13.10	+54:37:48.7	0.84	30.5	7.2	0.42 ± 0.09	0.12 ± 0.03	<0.40	−0.44 ± 0.17
N1_3	J161104.3+543107	16:11:04.33	+54:31:07.2	0.63	31.9	8.8	0.43 ± 0.08	0.12 ± 0.03	0.32 ± 0.12	0.04 ± 0.16
N1_4	J161059.5+543332	16:10:59.53	+54:33:32.4	0.45	122.5	31.6	1.62 ± 0.15	0.59 ± 0.06	1.13 ± 0.20	−0.35 ± 0.09
N1_5	J161058.1+543640	16:10:58.16	+54:36:40.7	0.47	60.6	18.5	0.81 ± 0.11	0.31 ± 0.05	0.58 ± 0.14	−0.41 ± 0.13
N1_6	J161055.7+543901	16:10:55.74	+54:39:01.0	0.47	195.6	43.7	2.64 ± 0.19	0.89 ± 0.08	2.23 ± 0.29	−0.25 ± 0.07
N1_8	J161055.5+543535	16:10:55.50	+54:35:35.6	0.44	125.9	34.8	1.72 ± 0.16	0.70 ± 0.07	0.96 ± 0.19	−0.54 ± 0.08
N1_9	J161055.0+543222	16:10:55.09	+54:32:22.3	0.50	56.6	16.2	0.74 ± 0.10	0.28 ± 0.04	0.52 ± 0.14	−0.40 ± 0.13
N1_10	J161052.3+542953	16:10:52.37	+54:29:53.8	0.63	12.6	4.1	0.17 ± 0.05	0.05 ± 0.02	<0.28	−0.27 ± 0.28
N1_11	J161051.6+543600	16:10:51.68	+54:36:00.9	0.57	27.0	7.9	0.35 ± 0.07	0.11 ± 0.03	0.36 ± 0.12	−0.09 ± 0.20
N1_12	J161050.7+542953	16:10:50.73	+54:29:53.9	0.61	30.8	8.5	0.41 ± 0.08	0.07 ± 0.02	0.61 ± 0.15	0.40 ± 0.18
N1_13	J161050.8+543956	16:10:50.85	+54:39:56.6	0.54	113.8	27.3	1.54 ± 0.15	0.58 ± 0.07	1.30 ± 0.22	−0.25 ± 0.09
N1_14	J161050.2+543024	16:10:50.21	+54:30:24.1	0.44	119.6	34.4	1.96 ± 0.18	0.73 ± 0.08	1.40 ± 0.25	−0.36 ± 0.09
N1_15	J161048.6+543553	16:10:48.64	+54:35:53.2	0.46	83.0	23.0	1.06 ± 0.12	0.45 ± 0.06	0.50 ± 0.14	−0.62 ± 0.09
N1_16	J161047.6+542813	16:10:47.68	+54:28:13.0	0.66	10.4	3.7	0.15 ± 0.05	<0.06	<0.32	0.60 ± 0.22
N1_17	J161047.5+543401	16:10:47.50	+54:34:01.9	0.66	12.4	4.0	0.16 ± 0.05	0.08 ± 0.02	<0.24	−0.75 ± 0.25
N1_18	J161047.2+543134	16:10:47.25	+54:31:34.7	0.63	18.7	5.8	0.24 ± 0.06	0.07 ± 0.02	<0.25	−0.23 ± 0.23
N1_19	J161047.0+543700	16:10:47.08	+54:37:00.8	0.52	50.9	14.1	0.66 ± 0.10	0.25 ± 0.04	0.40 ± 0.12	−0.46 ± 0.13
N1_20	J161046.5+543538	16:10:46.57	+54:35:38.8	0.69	18.2	5.4	0.23 ± 0.06	0.08 ± 0.03	<0.24	−0.34 ± 0.24
N1_21	J161046.0+542328	16:10:46.03	+54:23:28.5	0.73	126.9	18.9	1.87 ± 0.19	0.66 ± 0.08	1.10 ± 0.25	−0.44 ± 0.08
N1_22	J161045.1+542952	16:10:45.18	+54:29:52.6	0.61	18.6	5.7	0.24 ± 0.06	<0.05	0.54 ± 0.14	0.93 ± 0.20
N1_23	J161045.1+543612	16:10:45.15	+54:36:12.9	0.40	2826.1	569.9	36.00 ± 0.68	14.10 ± 0.31	22.46 ± 0.83	−0.43 ± 0.02
N1_24	J161044.1+542934	16:10:44.18	+54:29:34.1	0.70	18.9	5.5	0.24 ± 0.06	0.07 ± 0.02	<0.26	−0.12 ± 0.24
N1_25	J161044.1+543601	16:10:44.14	+54:36:01.9	0.42	148.2	41.5	1.88 ± 0.16	0.68 ± 0.07	1.45 ± 0.22	−0.31 ± 0.10
N1_26	J161042.8+542710	16:10:42.87	+54:27:10.2	0.68	24.6	7.1	0.33 ± 0.07	0.13 ± 0.03	<0.32	−0.54 ± 0.20
N1_27	J161041.6+542950	16:10:41.62	+54:29:50.1	0.69	19.9	6.2	0.30 ± 0.07	0.09 ± 0.03	<0.30	−0.34 ± 0.23
N1_28	J161041.3+543428	16:10:41.33	+54:34:28.4	0.55	8.8	3.2	0.11 ± 0.04	0.05 ± 0.02	<0.22	−1.00 ± 0.00
N1_29	J161040.2+543623	16:10:40.29	+54:36:23.3	0.48	25.9	8.7	0.33 ± 0.07	0.10 ± 0.03	0.36 ± 0.11	−0.19 ± 0.20
N1_30	J161040.1+544000	16:10:40.14	+54:40:00.9	0.54	70.9	18.7	0.95 ± 0.12	0.35 ± 0.05	0.77 ± 0.17	−0.29 ± 0.11
N1_31	J161039.1+543738	16:10:39.13	+54:37:38.5	0.48	61.2	17.1	0.78 ± 0.10	0.29 ± 0.05	0.49 ± 0.13	−0.45 ± 0.12
N1_32	J161038.1+543050	16:10:38.14	+54:30:50.3	0.49	15.5	5.5	0.19 ± 0.05	0.08 ± 0.02	<0.23	−0.83 ± 0.27
N1_34	J161035.4+543250	16:10:35.40	+54:32:50.7	0.46	39.8	13.3	0.50 ± 0.08	0.19 ± 0.04	0.32 ± 0.10	−0.48 ± 0.15
N1_38	J161033.6+543129	16:10:33.67	+54:31:29.9	0.44	15.2	5.8	0.19 ± 0.05	<0.04	0.32 ± 0.10	0.55 ± 0.26
N1_39	J161031.9+543204	16:10:31.97	+54:32:04.7	0.45	48.7	16.1	0.77 ± 0.11	0.23 ± 0.05	0.80 ± 0.18	−0.10 ± 0.15
N1_40	J161030.1+543142	16:10:30.12	+54:31:42.0	0.42	129.0	38.0	1.58 ± 0.14	0.57 ± 0.06	1.19 ± 0.19	−0.32 ± 0.08
N1_41	J161027.5+543022	16:10:27.59	+54:30:22.4	0.67	9.8	3.3	0.12 ± 0.04	<0.04	0.25 ± 0.09	0.87 ± 0.30
N1_43	J161026.7+543408	16:10:26.78	+54:34:08.1	0.50	13.7	5.0	0.17 ± 0.05	0.08 ± 0.02	<0.20	−0.92 ± 0.26
N1_45	J161023.2+543008	16:10:23.26	+54:30:08.7	0.50	45.3	13.6	0.59 ± 0.09	0.08 ± 0.02	1.00 ± 0.18	0.46 ± 0.18
N1_46	J161022.4+543149	16:10:22.45	+54:31:49.2	0.52	11.6	4.2	0.15 ± 0.05	<0.04	0.24 ± 0.09	0.40 ± 0.28
N1_47	J161022.1+543850	16:10:22.13	+54:38:50.8	0.46	80.3	22.7	1.02 ± 0.12	0.36 ± 0.05	0.77 ± 0.16	−0.31 ± 0.11
N1_48	J161021.7+543104	16:10:21.76	+54:31:04.7	0.41	260.8	71.9	3.17 ± 0.20	1.25 ± 0.09	1.89 ± 0.24	−0.44 ± 0.06
N1_49	J161020.8+543900	16:10:20.88	+54:39:00.9	0.46	87.0	25.6	1.11 ± 0.12	0.10 ± 0.03	2.21 ± 0.27	0.69 ± 0.09
N1_50	J161020.3+543020	16:10:20.34	+54:30:20.0	0.41	434.6	112.8	5.36 ± 0.26	2.20 ± 0.12	2.81 ± 0.29	−0.52 ± 0.04
N1_51	J161020.2+542937	16:10:20.25	+54:29:37.2	0.64	13.9	4.7	0.19 ± 0.06	<0.05	<0.24	0.03 ± 0.26
N1_52	J161019.9+544001	16:10:19.96	+54:40:01.8	0.68	23.1	6.8	0.32 ± 0.07	0.13 ± 0.03	<0.31	−0.44 ± 0.20
N1_53	J161018.8+543229	16:10:18.81	+54:32:29.5	0.61	10.7	3.6	0.13 ± 0.04	<0.04	<0.19	0.52 ± 0.29
N1_54	J161016.7+543136	16:10:16.78	+54:31:36.9	0.58	11.0	3.8	0.13 ± 0.05	<0.04	<0.20	0.35 ± 0.26
N1_55	J161015.1+543546	16:10:15.12	+54:35:46.4	0.51	27.6	9.1	0.33 ± 0.07	0.13 ± 0.03	<0.20	−0.39 ± 0.19
N1_56	J161014.6+542802	16:10:14.64	+54:28:02.2	0.63	25.0	7.4	0.32 ± 0.07	0.09 ± 0.03	0.37 ± 0.12	0.03 ± 0.23
N1_57	J161014.5+543754	16:10:14.57	+54:37:54.0	0.60	21.4	6.5	0.28 ± 0.07	0.09 ± 0.03	<0.25	−0.13 ± 0.23
N1_58	J161013.0+543459	16:10:13.07	+54:34:59.6	0.72	9.0	3.1	0.11 ± 0.04	<0.04	<0.20	0.46 ± 0.33
N1_59	J161012.8+542756	16:10:12.80	+54:27:56.5	0.43	219.2	53.6	2.84 ± 0.20	1.07 ± 0.09	1.91 ± 0.25	−0.38 ± 0.06
N1_60	J161012.3+543807	16:10:12.33	+54:38:07.9	0.60	21.0	6.6	0.28 ± 0.07	0.14 ± 0.03	<0.26	−1.00 ± 0.00
N1_61	J161009.5+543245	16:10:09.59	+54:32:45.6	0.58	26.3	7.9	0.32 ± 0.07	0.12 ± 0.03	0.23 ± 0.09	−0.44 ± 0.21
N1_62	J161009.0+543350	16:10:09.05	+54:33:50.9	0.42	39.8	16.6	1.12 ± 0.18	0.48 ± 0.08	0.51 ± 0.20	−0.68 ± 0.14
N1_64	J161008.1+543307	16:10:08.12	+54:33:07.7	0.44	51.7	17.2	0.63 ± 0.09	0.29 ± 0.04	0.22 ± 0.09	−0.89 ± 0.12
N1_65	J161007.4+543006	16:10:07.45	+54:30:06.8	0.54	25.2	8.7	0.48 ± 0.10	0.12 ± 0.03	0.59 ± 0.18	0.09 ± 0.20
N1_66	J161007.1+543722	16:10:07.16	+54:37:22.8	0.65	15.2	4.8	0.19 ± 0.05	0.09 ± 0.02	<0.24	−0.87 ± 0.25
N1_67	J161006.7+543243	16:10:06.77	+54:32:43.3	0.41	182.5	55.5	2.23 ± 0.17	0.88 ± 0.08	1.35 ± 0.20	−0.44 ± 0.07
N1_68	J161004.8+543513	16:10:04.88	+54:35:13.3	0.61	15.6	5.1	0.20 ± 0.06	0.08 ± 0.02	<0.22	−0.59 ± 0.26
N1_69	J161003.1+543628	16:10:03.18	+54:36:28.4	0.41	481.9	116.3	5.95 ± 0.27	2.30 ± 0.12	3.98 ± 0.35	−0.40 ± 0.04
N1_71	J161002.0+542525	16:10:02.03	+54:25:25.5	0.61	107.2	21.2	1.59 ± 0.16	0.61 ± 0.07	0.84 ± 0.19	−0.45 ± 0.09
N1_72	J161001.2+543752	16:10:01.26	+54:37:52.4	0.66	16.2	5.2	0.20 ± 0.06	<0.05	0.38 ± 0.12	0.70 ± 0.22

Table 1 – *continued*

ID	CXOEN1	RA (J2000)	Dec. (J2000)	Err (arcsec)	Net counts	S/N	Flux ($\times 10^{-14}$ erg cm^{-2} s^{-1}) (0.5–8 keV)	(0.5–2 keV)	(2–8 keV)	HR
N1_73	J161000.8+543918	16:10:00.86	+54:39:18.9	0.70	22.3	6.7	0.32 ± 0.07	0.06 ± 0.02	0.36 ± 0.12	0.25 ± 0.21
N1_75	J160959.6+543315	16:09:59.65	+54:33:15.2	0.43	125.4	35.7	1.62 ± 0.15	0.63 ± 0.07	0.96 ± 0.18	−0.46 ± 0.08
N1_76	J160959.0+542754	16:09:59.08	+54:27:54.1	0.63	15.5	6.2	0.49 ± 0.13	0.14 ± 0.05	0.56 ± 0.22	−0.27 ± 0.27
N1_77	J160956.9+543444	16:09:56.92	+54:34:44.5	0.62	14.3	5.6	0.34 ± 0.09	0.13 ± 0.04	<0.37	−0.97 ± 0.30
N1_78	J160956.7+543510	16:09:56.79	+54:35:10.3	0.47	26.6	8.8	0.38 ± 0.08	0.15 ± 0.03	0.26 ± 0.10	−0.46 ± 0.18
N1_79	J160956.0+543647	16:09:56.09	+54:36:47.4	0.55	14.0	4.8	0.18 ± 0.05	0.07 ± 0.02	<0.25	−0.69 ± 0.27
N1_81	J160952.2+543538	16:09:52.23	+54:35:38.6	0.47	45.0	14.2	0.58 ± 0.09	0.24 ± 0.04	0.28 ± 0.10	−0.62 ± 0.13
N1_82	J160951.0+542801	16:09:51.05	+54:28:01.9	0.55	70.4	18.1	0.95 ± 0.12	0.35 ± 0.05	0.59 ± 0.15	−0.49 ± 0.12
N1_83	J160951.0+543618	16:09:51.02	+54:36:18.8	0.62	34.7	9.5	0.48 ± 0.09	0.10 ± 0.03	0.62 ± 0.15	0.26 ± 0.17
N1_84	J160948.6+544307	16:09:48.68	+54:43:07.3	0.59	304.1	39.6	4.29 ± 0.26	1.57 ± 0.11	2.86 ± 0.36	−0.37 ± 0.06
N1_85	J160947.4+543147	16:09:47.46	+54:31:47.0	0.61	13.0	4.4	0.17 ± 0.05	<0.05	<0.25	0.01 ± 0.29
N1_86	J160943.8+543749	16:09:43.88	+54:37:49.3	0.71	28.8	7.6	0.38 ± 0.08	0.11 ± 0.03	0.39 ± 0.12	−0.06 ± 0.18
N1_87	J160941.0+544013	16:09:41.08	+54:40:13.1	0.58	147.1	26.0	1.99 ± 0.18	0.78 ± 0.08	1.18 ± 0.22	−0.46 ± 0.08
N1_89	J160937.2+544032	16:09:37.20	+54:40:32.6	0.51	307.8	47.6	4.31 ± 0.26	1.56 ± 0.11	3.22 ± 0.37	−0.28 ± 0.05
N1_90	J160936.2+543812	16:09:36.24	+54:38:12.5	0.58	80.9	18.2	1.08 ± 0.13	0.45 ± 0.06	0.49 ± 0.15	−0.47 ± 0.11
N1_92	J160933.9+543652	16:09:33.97	+54:36:52.3	0.58	47.1	12.5	0.62 ± 0.10	0.09 ± 0.03	1.13 ± 0.21	0.43 ± 0.12
N1_93	J160932.8+543210	16:09:32.83	+54:32:10.4	0.49	118.5	28.1	1.58 ± 0.15	0.58 ± 0.06	1.18 ± 0.21	−0.34 ± 0.09
N1_94	J160932.3+543155	16:09:32.31	+54:31:55.5	0.66	44.9	10.9	0.60 ± 0.10	0.21 ± 0.04	<0.32	−0.27 ± 0.16
N1_95	J160916.3+543211	16:09:16.33	+54:32:11.1	0.79	44.7	9.7	0.63 ± 0.11	0.21 ± 0.04	<0.43	−0.32 ± 0.13
N1_96	J161120.3+543508	16:11:20.30	+54:35:08.4	0.73	32.3	7.9	0.45 ± 0.09	<0.07	1.16 ± 0.22	1.00 ± 0.00
N1_97	J161108.3+543250	16:11:08.38	+54:32:50.6	0.64	29.0	8.5	0.39 ± 0.08	0.18 ± 0.04	<0.32	−0.64 ± 0.19
N1_98	J161107.0+543538	16:11:07.08	+54:35:38.6	0.71	16.2	5.2	0.22 ± 0.06	0.07 ± 0.02	<0.32	−0.14 ± 0.23
N1_99	J161102.8+542959	16:11:02.81	+54:29:59.5	0.68	43.4	11.1	0.70 ± 0.12	0.14 ± 0.03	0.53 ± 0.16	−0.16 ± 0.16
N1_100	J161102.0+543826	16:11:02.02	+54:38:26.7	0.76	23.3	6.6	0.32 ± 0.07	0.12 ± 0.03	<0.36	−0.12 ± 0.18
N1_101	J161051.9+543006	16:10:51.99	+54:30:06.9	0.66	12.7	4.2	0.17 ± 0.05	<0.05	<0.28	0.11 ± 0.31
N1_102	J161051.6+543446	16:10:51.62	+54:34:46.9	0.69	14.3	4.6	0.18 ± 0.05	<0.05	0.34 ± 0.11	0.69 ± 0.24
N1_103	J161048.2+542547	16:10:48.20	+54:25:47.9	0.87	24.8	6.0	0.35 ± 0.08	0.10 ± 0.03	<0.40	0.05 ± 0.19
N1_104	J161046.6+542437	16:10:46.63	+54:24:37.5	0.72	74.6	14.5	1.14 ± 0.15	0.48 ± 0.06	0.64 ± 0.19	−0.39 ± 0.11
N1_106	J161017.4+543149	16:10:17.40	+54:31:49.2	0.72	11.5	3.8	0.14 ± 0.05	<0.04	<0.20	0.21 ± 0.29
N1_107	J161011.9+543352	16:10:11.98	+54:33:52.5	0.67	8.8	3.2	0.13 ± 0.05	<0.05	<0.22	−1.00 ± 0.00
N1_108	J161004.9+542636	16:10:04.99	+54:26:36.9	0.65	40.4	11.5	0.64 ± 0.11	0.23 ± 0.05	<0.39	−0.42 ± 0.16
N1_110	J160951.7+543358	16:09:51.79	+54:33:58.1	0.75	10.8	3.6	0.14 ± 0.05	<0.05	0.30 ± 0.10	1.00 ± 0.00
N1_111	J160948.7+542647	16:09:48.71	+54:26:47.1	0.61	28.6	8.8	0.40 ± 0.08	0.17 ± 0.04	<0.37	−0.41 ± 0.16
N1_112	J160948.2+543611	16:09:48.20	+54:36:11.3	0.70	17.9	5.2	0.24 ± 0.06	<0.05	0.47 ± 0.14	0.80 ± 0.20
N1_113	J161126.3+543528	16:11:26.36	+54:35:28.7	1.06	32.1	6.7	0.51 ± 0.11	0.15 ± 0.04	0.46 ± 0.16	−0.16 ± 0.16
N1_114	J161103.8+543303	16:11:03.83	+54:33:03.1	0.81	15.2	4.5	0.21 ± 0.06	<0.06	<0.31	0.05 ± 0.22
N1_115	J161029.8+542401	16:10:29.86	+54:24:01.6	0.88	23.3	6.0	0.38 ± 0.09	0.16 ± 0.04	<0.49	−0.56 ± 0.18
N1_116	J161021.6+542608	16:10:21.67	+54:26:08.0	0.89	11.4	3.7	0.17 ± 0.06	<0.06	<0.34	0.80 ± 0.19
N1_117	J161018.4+542733	16:10:18.49	+54:27:33.4	0.77	18.5	5.3	0.24 ± 0.06	<0.05	<0.28	0.20 ± 0.22
N1_118	J161005.2+543909	16:10:05.23	+54:39:09.7	0.85	13.6	4.1	0.17 ± 0.05	<0.05	<0.28	−0.22 ± 0.26
N1_119	J160953.7+543755	16:09:53.78	+54:37:55.6	0.68	12.8	4.3	0.17 ± 0.05	<0.06	0.33 ± 0.12	0.72 ± 0.19
N1_121	J160932.6+543436	16:09:32.63	+54:34:36.9	0.78	13.1	4.2	0.18 ± 0.06	<0.06	0.56 ± 0.15	0.80 ± 0.14
N1_123	J161137.0+542541	16:11:37.00	+54:25:41.6	0.99	136.6	12.4	2.11 ± 0.24	0.56 ± 0.08	2.81 ± 0.49	0.15 ± 0.07
N1_124	J161131.4+543706	16:11:31.40	+54:37:06.2	1.28	18.1	3.9	0.29 ± 0.09	0.15 ± 0.04	<0.62	−0.39 ± 0.19
N1_125	J161123.7+542632	16:11:23.71	+54:26:32.7	0.99	85.2	9.7	1.22 ± 0.17	0.29 ± 0.06	1.74 ± 0.35	0.36 ± 0.09
N1_126	J161122.0+542217	16:11:22.00	+54:22:17.0	1.13	214.9	12.7	3.27 ± 0.33	1.14 ± 0.12	2.66 ± 0.53	−0.10 ± 0.06
N1_127	J161101.6+543030	16:11:01.64	+54:30:30.3	0.78	12.0	4.1	0.21 ± 0.07	0.09 ± 0.03	<0.38	−0.54 ± 0.24
N1_128	J161043.4+543403	16:10:43.44	+54:34:03.9	0.72	12.8	4.0	0.16 ± 0.05	0.07 ± 0.02	<0.23	−0.38 ± 0.27
N1_129	J161025.7+542328	16:10:25.78	+54:23:28.4	1.01	43.2	9.0	0.93 ± 0.17	0.47 ± 0.09	<0.60	−0.91 ± 0.11
N1_131	J160943.6+543849	16:09:43.63	+54:38:49.9	0.80	14.1	4.4	0.19 ± 0.06	0.07 ± 0.02	<0.34	−0.05 ± 0.18
N1_132	J160920.4+543103	16:09:20.49	+54:31:03.3	0.82	15.9	4.6	0.23 ± 0.07	0.06 ± 0.02	0.32 ± 0.13	0.00 ± 0.18
N1_133	J160916.9+542811	16:09:16.98	+54:28:11.1	0.99	33.5	6.5	0.51 ± 0.11	0.11 ± 0.03	0.68 ± 0.22	0.25 ± 0.13
N1_135	J161132.0+542309	16:11:32.03	+54:23:09.1	1.30	197.5	11.2	3.08 ± 0.34	1.27 ± 0.13	–	−0.26 ± 0.07
N1_136	J161007.7+543834	16:10:07.74	+54:38:34.4	0.79	16.1	4.8	0.22 ± 0.06	0.07 ± 0.03	<0.28	−0.23 ± 0.24
N1_137	J161101.6+543422	16:11:01.64	+54:34:22.9	0.80	11.7	3.6	0.15 ± 0.05	<0.05	0.31 ± 0.11	0.46 ± 0.26
N1_138	J161109.3+542035	16:11:09.31	+54:20:35.4	1.42	62.6	5.0	0.96 ± 0.22	0.40 ± 0.08	–	−0.10 ± 0.08
N1_139	J160942.5+542709	16:09:42.56	+54:27:09.1	0.97	17.4	4.7	0.24 ± 0.07	0.10 ± 0.03	<0.38	−0.34 ± 0.20
N1_140	J161058.4+543852	16:10:58.45	+54:38:52.5	0.91	14.0	4.4	0.19 ± 0.06	0.08 ± 0.03	<0.35	−0.66 ± 0.28
N1_141	J160943.1+544152	16:09:43.19	+54:41:52.3	1.20	18.4	4.0	0.26 ± 0.08	0.11 ± 0.03	<0.48	−1.00 ± 0.00
N1_142	J161113.5+543612	16:11:13.53	+54:36:12.6	0.99	13.7	3.7	0.20 ± 0.06	0.07 ± 0.03	<0.39	−0.96 ± 0.26
N1_143	J160940.1+543713	16:09:40.15	+54:37:13.5	0.82	11.2	3.6	0.15 ± 0.05	<0.06	0.35 ± 0.12	1.00 ± 0.00
N1_144	J160941.8+543127	16:09:41.83	+54:31:27.5	0.77	10.1	3.4	0.14 ± 0.05	<0.06	0.34 ± 0.12	1.00 ± 0.00
N1_145	J161048.8+543205	16:10:48.84	+54:32:05.9	0.78	9.5	3.1	0.12 ± 0.05	<0.05	<0.25	−0.25 ± 0.31

Table 1 – *continued*

ID	CXOEN1	RA (J2000)	Dec. (J2000)	Err (arcsec)	Net counts	S/N	Flux ($\times10^{-14}$ erg cm^{-2} s^{-1}) (0.5–8 keV)	(0.5–2 keV)	(2–8 keV)	HR
N1_146	J160946.1+543624	16:09:46.18	+54:36:24.5	0.74	12.0	3.8	0.15 ± 0.05	0.06 ± 0.02	<0.27	-0.18 ± 0.26
N1_147	J160909.8+542841	16:09:09.89	+54:28:41.4	1.67	10.9	3.2	<0.31	0.09 ± 0.03	<0.66	-0.19 ± 0.17
N1_148	J161037.9+543336	16:10:37.92	+54:33:36.9	0.67	7.1	3.1	<0.11	0.05 ± 0.02	<0.21	-0.36 ± 0.31
N1_149	J160923.1+542810	16:09:23.15	+54:28:10.4	1.01	10.2	3.0	<0.20	<0.08	0.36 ± 0.14	1.00 ± 0.00

Table 2. *Chandra* sources in the ELAIS N2 field.

ID	CXOEN2	RA (J2000)	Dec. (J2000)	Err (arcsec)	Net counts	S/N	Flux ($\times10^{-14}$ erg cm^{-2} s^{-1}) (0.5–8 keV)	(0.5–2 keV)	(2–8 keV)	HR
N2_1	J163733.4+410309	16:37:33.41	+41:03:09.3	0.44	638.9	101.7	8.73 ± 0.35	3.20 ± 0.15	6.32 ± 0.48	-0.33 ± 0.04
N2_2	J163730.2+410049	16:37:30.27	+41:00:49.8	0.71	52.6	11.0	0.71 ± 0.11	0.16 ± 0.04	0.77 ± 0.18	0.17 ± 0.12
N2_4	J163720.5+410402	16:37:20.50	+41:04:02.2	0.59	11.6	4.2	0.17 ± 0.05	0.06 ± 0.02	<0.32	-0.55 ± 0.28
N2_5	J163720.5+410626	16:37:20.58	+41:06:26.6	0.49	216.6	45.4	2.87 ± 0.20	0.99 ± 0.08	2.33 ± 0.29	-0.24 ± 0.07
N2_6	J163715.2+410443	16:37:15.24	+41:04:43.1	0.58	18.8	6.3	0.24 ± 0.06	0.08 ± 0.02	<0.28	-0.23 ± 0.22
N2_7	J163712.3+410139	16:37:12.38	+41:01:39.2	0.43	94.0	29.6	1.29 ± 0.14	0.48 ± 0.06	0.99 ± 0.19	-0.35 ± 0.10
N2_8	J163712.3+410131	16:37:12.36	+41:01:31.7	0.54	15.6	5.6	0.21 ± 0.06	0.08 ± 0.02	<0.26	-0.40 ± 0.25
N2_9	J163710.0+405643	16:37:10.04	+40:56:43.2	0.43	338.9	73.8	4.74 ± 0.26	1.97 ± 0.12	2.39 ± 0.30	-0.52 ± 0.05
N2_10	J163709.2+410457	16:37:09.20	+41:04:57.5	0.52	41.0	12.1	0.51 ± 0.09	0.21 ± 0.04	0.26 ± 0.10	-0.47 ± 0.15
N2_11	J163706.7+410501	16:37:06.72	+41:05:01.7	0.77	10.1	3.5	0.13 ± 0.05	<0.05	<0.25	-0.78 ± 0.37
N2_12	J163706.0+410054	16:37:06.00	+41:00:54.6	0.57	10.4	3.7	0.13 ± 0.04	<0.05	<0.23	0.11 ± 0.33
N2_13	J163705.0+405749	16:37:05.03	+40:57:49.2	0.61	19.7	6.1	0.25 ± 0.06	<0.05	0.57 ± 0.14	0.82 ± 0.16
N2_14	J163704.9+410509	16:37:04.94	+41:05:09.0	0.44	95.4	28.8	1.19 ± 0.12	0.29 ± 0.04	1.50 ± 0.22	0.11 ± 0.10
N2_15	J163704.4+405625	16:37:04.41	+40:56:25.1	0.63	15.6	5.2	0.22 ± 0.06	0.08 ± 0.03	<0.31	-0.18 ± 0.23
N2_16	J163703.2+410103	16:37:03.27	+41:01:03.3	0.48	11.8	4.3	0.14 ± 0.05	0.06 ± 0.02	<0.22	-0.48 ± 0.30
N2_17	J163703.1+405157	16:37:03.15	+40:51:57.0	0.66	180.1	25.0	2.57 ± 0.21	0.65 ± 0.07	3.04 ± 0.37	0.12 ± 0.07
N2_18	J163700.6+410555	16:37:00.64	+41:05:55.7	0.42	251.7	69.1	3.13 ± 0.20	1.25 ± 0.09	1.85 ± 0.24	-0.45 ± 0.06
N2_19	J163658.8+405727	16:36:58.82	+40:57:27.8	0.54	23.3	7.5	0.32 ± 0.07	0.09 ± 0.03	0.41 ± 0.12	0.14 ± 0.21
N2_20	J163658.3+410537	16:36:58.31	+41:05:37.1	0.49	31.2	9.9	0.38 ± 0.07	0.12 ± 0.03	0.41 ± 0.12	-0.06 ± 0.18
N2_21	J163658.0+405821	16:36:58.07	+40:58:21.1	0.41	175.2	52.2	2.15 ± 0.16	0.83 ± 0.07	1.39 ± 0.21	-0.42 ± 0.07
N2_22	J163656.6+410449	16:36:56.63	+41:04:49.7	0.47	34.4	11.1	0.42 ± 0.08	0.17 ± 0.03	0.24 ± 0.09	-0.53 ± 0.16
N2_23	J163656.0+410625	16:36:56.04	+41:06:25.1	0.67	11.1	3.8	0.15 ± 0.05	<0.05	0.38 ± 0.12	1.00 ± 0.00
N2_24	J163655.7+405652	16:36:55.72	+40:56:52.4	0.46	97.2	25.9	1.27 ± 0.13	0.32 ± 0.05	1.53 ± 0.23	0.09 ± 0.10
N2_25	J163655.7+405910	16:36:55.79	+40:59:10.5	0.43	84.7	24.5	1.02 ± 0.11	0.21 ± 0.04	1.47 ± 0.21	0.26 ± 0.11
N2_26	J163655.5+410809	16:36:55.56	+41:08:09.9	0.61	49.2	13.2	0.63 ± 0.10	0.28 ± 0.04	<0.30	-0.61 ± 0.14
N2_27	J163655.3+410714	16:36:55.37	+41:07:14.7	0.64	28.2	8.4	0.39 ± 0.08	0.14 ± 0.03	<0.29	-0.44 ± 0.19
N2_28	J163655.2+405944	16:36:55.21	+40:59:44.1	0.47	32.1	11.0	0.38 ± 0.07	0.11 ± 0.03	0.38 ± 0.11	-0.14 ± 0.18
N2_29	J163655.1+410152	16:36:55.16	+41:01:52.4	0.55	14.2	4.9	0.17 ± 0.05	0.06 ± 0.02	<0.20	-0.23 ± 0.28
N2_32	J163653.2+405917	16:36:53.26	+40:59:17.3	0.55	10.7	3.9	0.13 ± 0.04	<0.04	0.28 ± 0.10	0.96 ± 0.30
N2_33	J163651.6+405600	16:36:51.69	+40:56:00.4	0.69	24.0	6.7	0.31 ± 0.07	<0.05	0.52 ± 0.14	0.37 ± 0.19
N2_34	J163650.6+405840	16:36:50.63	+40:58:40.6	0.47	35.9	11.2	0.43 ± 0.08	0.14 ± 0.03	0.39 ± 0.11	-0.20 ± 0.17
N2_35	J163649.1+410324	16:36:49.18	+41:03:24.3	0.83	16.2	5.7	0.44 ± 0.12	<0.09	<0.39	0.16 ± 0.32
N2_37	J163647.3+410659	16:36:47.30	+41:06:59.0	0.50	60.2	16.9	0.78 ± 0.10	0.17 ± 0.04	1.10 ± 0.19	0.21 ± 0.13
N2_38	J163647.1+410334	16:36:47.15	+41:03:34.8	0.42	142.6	41.1	1.79 ± 0.15	0.76 ± 0.07	0.85 ± 0.17	-0.59 ± 0.07
N2_39	J163646.5+405729	16:36:46.57	+40:57:29.1	0.53	21.4	6.9	0.26 ± 0.06	0.11 ± 0.03	<0.23	-0.51 ± 0.21
N2_40	J163645.5+410313	16:36:45.51	+41:03:13.9	0.51	25.4	8.2	0.32 ± 0.07	0.09 ± 0.03	0.33 ± 0.11	-0.06 ± 0.22
N2_41	J163644.7+405540	16:36:44.73	+40:55:40.6	0.45	139.9	35.2	1.79 ± 0.16	0.76 ± 0.07	0.69 ± 0.16	-0.58 ± 0.07
N2_42	J163644.6+405643	16:36:44.68	+40:56:43.6	0.56	32.7	9.5	0.41 ± 0.08	0.17 ± 0.03	<0.25	-0.61 ± 0.17
N2_43	J163642.7+405514	16:36:42.71	+40:55:14.9	0.58	46.7	12.8	0.60 ± 0.09	0.23 ± 0.04	<0.29	-0.34 ± 0.15
N2_44	J163641.3+405550	16:36:41.35	+40:55:50.2	0.48	80.9	21.3	1.03 ± 0.12	0.35 ± 0.05	0.86 ± 0.17	-0.27 ± 0.11
N2_46	J163639.3+410259	16:36:39.34	+41:02:59.5	0.55	13.2	4.6	0.15 ± 0.05	0.05 ± 0.02	<0.19	-0.51 ± 0.30
N2_47	J163636.2+410509	16:36:36.21	+41:05:09.5	0.46	31.5	10.3	0.38 ± 0.07	0.15 ± 0.03	0.27 ± 0.10	-0.45 ± 0.18
N2_48	J163633.6+410534	16:36:33.66	+41:05:34.3	0.45	76.6	22.0	0.93 ± 0.11	0.40 ± 0.05	0.52 ± 0.13	-0.53 ± 0.11
N2_51	J163630.5+405651	16:36:30.54	+40:56:51.8	0.44	291.5	72.1	6.09 ± 0.37	1.58 ± 0.14	7.54 ± 0.65	0.09 ± 0.06
N2_52	J163629.7+410222	16:36:29.71	+41:02:22.7	0.41	312.1	79.2	3.78 ± 0.22	1.42 ± 0.10	2.60 ± 0.28	-0.38 ± 0.05
N2_54	J163628.1+405527	16:36:28.13	+40:55:27.5	0.42	604.8	121.2	7.92 ± 0.33	2.93 ± 0.14	5.78 ± 0.44	-0.33 ± 0.04
N2_55	J163627.4+410615	16:36:27.47	+41:06:15.4	0.73	18.3	5.5	0.23 ± 0.06	<0.05	0.34 ± 0.11	0.49 ± 0.21
N2_56	J163625.4+405741	16:36:25.46	+40:57:41.4	0.46	138.3	34.0	1.77 ± 0.16	0.75 ± 0.07	0.76 ± 0.16	-0.57 ± 0.07
N2_57	J163623.0+410015	16:36:23.07	+41:00:15.0	0.52	32.8	10.2	0.41 ± 0.08	0.17 ± 0.03	0.25 ± 0.09	-0.51 ± 0.16
N2_58	J163622.5+410641	16:36:22.54	+41:06:41.6	0.56	59.6	14.8	0.76 ± 0.11	0.39 ± 0.05	<0.30	-1.00 ± 0.00
N2_59	J163622.4+410927	16:36:22.49	+41:09:27.7	0.61	104.7	20.0	1.39 ± 0.15	0.55 ± 0.06	0.74 ± 0.19	-0.39 ± 0.09
N2_60	J163619.2+410436	16:36:19.23	+41:04:36.9	0.52	51.0	14.2	0.65 ± 0.10	0.26 ± 0.04	<0.28	-0.58 ± 0.13
N2_61	J163618.2+410038	16:36:18.23	+41:00:38.6	0.57	38.5	11.0	0.52 ± 0.09	0.18 ± 0.04	0.39 ± 0.12	-0.39 ± 0.17

Table 2 – *continued*

ID	CXOEN2	RA (J2000)	Dec. (J2000)	Err (arcsec)	Net counts	S/N	Flux ($\times 10^{-14}$ erg cm^{-2} s^{-1}) (0.5–8 keV)	(0.5–2 keV)	(2–8 keV)	HR
N2_62	J163616.4+405748	16:36:16.42	+40:57:48.3	0.59	29.9	8.8	0.39 ± 0.08	0.16 ± 0.03	<0.31	−0.35 ± 0.17
N2_63	J163615.6+405716	16:36:15.60	+40:57:16.6	0.71	20.3	6.1	0.27 ± 0.07	0.09 ± 0.03	<0.32	−0.91 ± 0.21
N2_64	J163614.4+410349	16:36:14.46	+41:03:49.1	0.53	78.0	19.0	1.00 ± 0.12	0.37 ± 0.05	0.72 ± 0.16	−0.38 ± 0.11
N2_65	J163612.1+410242	16:36:12.16	+41:02:42.7	0.62	39.5	10.7	0.51 ± 0.09	0.20 ± 0.04	<0.30	−0.52 ± 0.16
N2_66	J163606.7+410440	16:36:06.79	+41:04:40.0	0.71	79.4	15.0	1.17 ± 0.15	0.34 ± 0.05	1.15 ± 0.23	0.01 ± 0.11
N2_67	J163555.7+410054	16:35:55.72	+41:00:54.5	0.95	53.1	8.9	0.79 ± 0.13	0.23 ± 0.05	0.53 ± 0.17	−0.34 ± 0.14
N2_68	J163725.2+410021	16:37:25.26	+41:00:21.1	0.69	17.5	5.3	0.23 ± 0.06	0.08 ± 0.03	<0.33	−0.56 ± 0.22
N2_71	J163710.8+405402	16:37:10.81	+40:54:02.4	0.77	30.7	7.1	0.42 ± 0.09	0.13 ± 0.03	<0.40	0.09 ± 0.15
N2_72	J163657.7+410021	16:36:57.74	+41:00:21.5	0.73	11.9	3.7	0.15 ± 0.05	0.08 ± 0.02	<0.21	−0.92 ± 0.26
N2_73	J163635.8+405325	16:36:35.86	+40:53:25.6	0.78	46.1	9.8	0.62 ± 0.10	0.19 ± 0.04	0.35 ± 0.13	−0.08 ± 0.14
N2_74	J163632.9+411111	16:36:32.95	+41:11:11.4	0.88	53.2	10.0	0.72 ± 0.11	0.29 ± 0.05	<0.46	−0.40 ± 0.11
N2_75	J163632.7+410513	16:36:32.78	+41:05:13.7	0.69	20.4	6.2	0.25 ± 0.06	<0.05	0.32 ± 0.11	0.30 ± 0.22
N2_76	J163632.6+410552	16:36:32.64	+41:05:52.7	0.65	12.7	4.2	0.15 ± 0.05	0.05 ± 0.02	<0.25	−0.22 ± 0.30
N2_77	J163625.2+410228	16:36:25.25	+41:02:28.2	0.68	12.3	3.9	0.15 ± 0.05	<0.05	0.31 ± 0.11	1.00 ± 0.00
N2_78	J163624.1+410821	16:36:24.12	+41:08:21.2	0.77	36.3	8.3	0.47 ± 0.09	0.17 ± 0.04	<0.35	−0.29 ± 0.16
N2_79	J163620.6+405714	16:36:20.68	+40:57:14.8	0.75	24.7	7.1	0.32 ± 0.07	<0.06	0.55 ± 0.14	0.66 ± 0.15
N2_80	J163617.9+405636	16:36:17.96	+40:56:36.5	0.72	30.1	8.0	0.40 ± 0.08	0.08 ± 0.03	0.39 ± 0.12	−0.11 ± 0.18
N2_81	J163731.1+410410	16:37:31.15	+41:04:10.8	0.87	21.7	5.4	0.31 ± 0.08	0.09 ± 0.03	<0.41	−0.24 ± 0.18
N2_82	J163718.1+410600	16:37:18.16	+41:06:00.1	0.72	11.0	3.7	0.14 ± 0.05	0.05 ± 0.02	<0.32	−0.00 ± 0.22
N2_83	J163717.6+410324	16:37:17.66	+41:03:24.1	0.83	11.7	3.9	0.17 ± 0.06	0.09 ± 0.03	<0.32	−0.73 ± 0.28
N2_84	J163708.3+410526	16:37:08.37	+41:05:26.0	0.72	11.2	3.9	0.15 ± 0.05	<0.05	<0.27	0.13 ± 0.29
N2_85	J163648.0+410354	16:36:48.04	+41:03:54.9	0.71	10.8	3.6	0.14 ± 0.05	<0.04	0.27 ± 0.10	0.84 ± 0.28
N2_86	J163633.7+411102	16:36:33.71	+41:11:02.4	0.83	42.6	9.0	0.61 ± 0.11	0.19 ± 0.04	0.76 ± 0.20	−0.21 ± 0.12
N2_87	J163627.6+405416	16:36:27.62	+40:54:16.1	0.99	20.8	5.0	0.30 ± 0.08	0.10 ± 0.03	<0.37	−0.39 ± 0.20
N2_88	J163616.0+405500	16:36:16.01	+40:55:00.9	0.82	57.2	11.9	0.94 ± 0.14	0.30 ± 0.06	0.62 ± 0.18	0.06 ± 0.11
N2_89	J163615.0+405639	16:36:15.03	+40:56:39.3	0.81	18.5	5.3	0.26 ± 0.07	0.07 ± 0.02	<0.36	0.07 ± 0.20
N2_90	J163612.3+410731	16:36:12.34	+41:07:31.3	0.81	48.7	9.5	0.66 ± 0.11	0.18 ± 0.04	0.38 ± 0.13	0.01 ± 0.13
N2_91	J163604.3+405646	16:36:04.31	+40:56:46.8	0.99	22.9	5.5	0.32 ± 0.08	0.09 ± 0.03	<0.43	0.27 ± 0.17
N2_92	J163559.3+410116	16:35:59.30	+41:01:16.0	0.73	14.7	4.3	0.21 ± 0.06	0.09 ± 0.03	<0.43	−0.75 ± 0.17
N2_93	J163735.5+410448	16:37:35.54	+41:04:48.9	0.97	28.4	6.5	0.39 ± 0.09	0.13 ± 0.03	<0.45	−0.33 ± 0.15
N2_94	J163734.5+405046	16:37:34.51	+40:50:46.7	0.95	395.9	22.4	5.92 ± 0.39	1.78 ± 0.14	5.54 ± 0.67	−0.02 ± 0.05
N2_96	J163608.4+410404	16:36:08.45	+41:04:04.1	0.73	13.3	4.2	0.19 ± 0.06	0.08 ± 0.02	<0.36	−0.43 ± 0.22
N2_97	J163602.6+405927	16:36:02.66	+40:59:27.3	1.03	26.0	5.7	0.35 ± 0.08	<0.07	<0.39	−0.09 ± 0.18
N2_98	J163623.4+410859	16:36:23.47	+41:08:59.0	0.88	27.9	6.3	0.37 ± 0.08	0.06 ± 0.02	0.40 ± 0.13	0.60 ± 0.17
N2_99	J163734.5+405212	16:37:34.56	+40:52:12.8	1.12	108.3	8.5	1.53 ± 0.22	0.59 ± 0.08	–	−0.01 ± 0.08
N2_100	J163729.9+405349	16:37:29.99	+40:53:49.3	1.04	23.9	4.1	0.34 ± 0.10	0.20 ± 0.05	–	−0.01 ± 0.12
N2_101	J163633.8+410731	16:36:33.84	+41:07:31.0	0.86	15.4	4.7	0.21 ± 0.06	<0.06	<0.30	−0.47 ± 0.26
N2_102	J163725.6+405811	16:37:25.68	+40:58:11.0	0.83	12.4	4.9	0.47 ± 0.14	0.19 ± 0.06	<0.69	−0.49 ± 0.27
N2_103	J163639.9+405322	16:36:39.97	+40:53:22.8	0.98	14.1	4.2	0.19 ± 0.06	<0.06	<0.38	0.41 ± 0.17
N2_104	J163640.7+410449	16:36:40.77	+41:04:49.8	0.76	10.6	3.5	0.13 ± 0.05	<0.05	<0.22	0.45 ± 0.31
N2_105	J163640.9+410840	16:36:40.90	+41:08:40.7	0.71	12.3	4.0	0.16 ± 0.05	<0.06	<0.31	0.63 ± 0.21
N2_106	J163642.3+410520	16:36:42.33	+41:05:20.8	0.75	11.1	3.5	0.14 ± 0.05	0.05 ± 0.02	<0.23	−0.42 ± 0.29
N2_107	J163608.4+410507	16:36:08.41	+41:05:07.0	0.86	12.1	3.4	0.18 ± 0.06	0.10 ± 0.03	<0.39	−0.26 ± 0.22
N2_108	J163613.4+405806	16:36:13.45	+40:58:06.4	0.82	9.7	3.2	0.13 ± 0.05	<0.06	<0.32	−0.13 ± 0.25
N2_109	J163730.7+405152	16:37:30.77	+40:51:52.6	1.23	31.2	3.9	0.44 ± 0.13	–	–	0.34 ± 0.09
N2_110	J163708.0+410840	16:37:08.04	+41:08:40.1	1.31	8.3	3.2	<0.20	0.08 ± 0.03	<0.48	−0.40 ± 0.28
N2_111	J163627.5+410228	16:36:27.50	+41:02:28.6	0.59	7.1	3.2	<0.11	0.05 ± 0.02	<0.23	−1.00 ± 0.00
N2_112	J163723.8+410133	16:37:23.83	+41:01:33.3	0.88	7.6	3.1	<0.14	0.06 ± 0.02	<0.32	−0.41 ± 0.26
N2_113	J163621.4+410049	16:36:21.42	+41:00:49.9	0.98	10.0	3.4	<0.12	<0.05	0.30 ± 0.11	1.00 ± 0.00
N2_114	J163631.8+410432	16:36:31.82	+41:04:32.7	0.59	7.6	3.1	<0.12	<0.05	0.24 ± 0.09	0.52 ± 0.31

5.1 Calculating source counts

$N(>S)$ is defined as the sum of the reciprocal areas available for detecting each source that is brighter than flux S. It follows that $n(S)$ is the sum of reciprocal areas per flux interval. The sky area over which a source of flux S may be observed depends on the flux limit at each point in the image. This, in turn, depends on the variation in PSF size and effective exposure across the image. The flux limit ($S_{\rm lim}$ in erg cm^{-2} s^{-1}) may be defined by the chosen S/N limit of our sample (from equation 1):

$$S/N_{\rm lim} = 3 = C_{\rm lim}/(1 + \sqrt{0.75 + B}) \quad (2)$$

where

$$C_{\rm lim} = S_{\rm lim} \times \text{effective exposure} \times K. \quad (3)$$

K is a constant (conversion factor from erg to counts), while the effective exposure (in cm^2) at each point on the image can be found from the exposure map. The background counts within the source

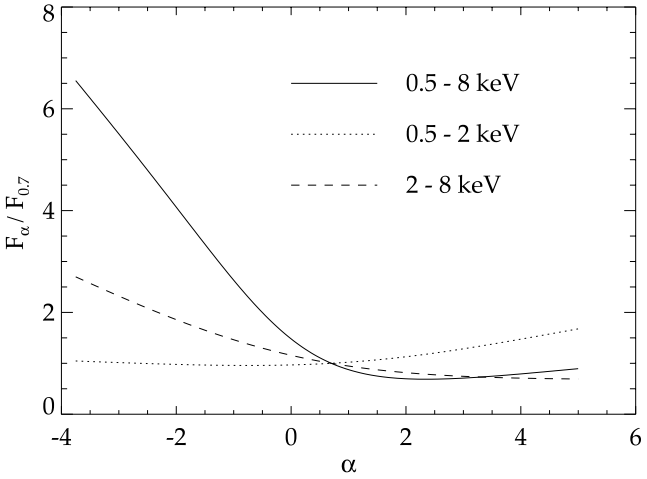

Figure 2. Conversion factors to calculate true flux for a source with spectral slope α given the fluxes quoted in the source catalogue (which assumes $\alpha = 0.7$). This figure has been calculated by passing model spectra of slope α through the total response matrix of the detector at a position corresponding to the source N1_23.

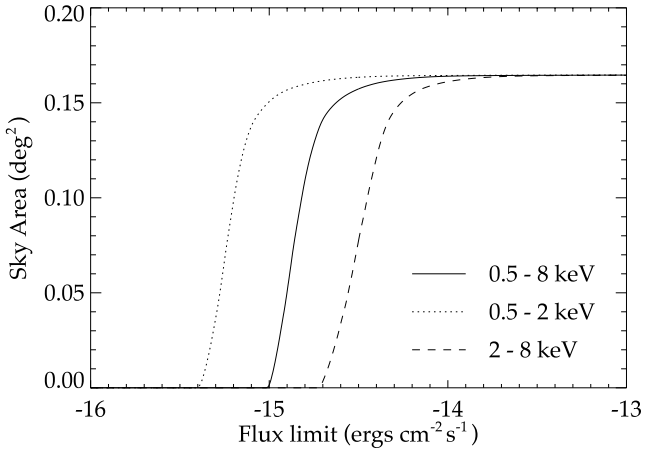

Figure 3. Sky area observed at survey flux limit.

region (B) depend on the size of the PSF:

$$B = B_{\rm avg} \times \text{PSF size}. \quad (4)$$

$B_{\rm avg}$ is the mean background counts per pixel. We are left with the following expression for the flux limit:

$$S_{\rm lim} = 3 \times \frac{1 + \sqrt{0.75 + (B_{\rm avg} \times \text{PSF size})}}{\text{effective exposure} \times K}. \quad (5)$$

PSF sizes across the image were taken from the latest PSF library available with the CIAO software distribution. These were used in conjunction with the relevant exposure maps for each band to calculate a 'flux limit map' of the *Chandra* image. The sky area available at a given flux limit is found by summing all the pixels with values smaller than this limit. Fig. 3 displays the sky area available at the flux limit of our survey.

5.2 Results

The cumulative number counts per deg^2 are plotted as filled circles in Fig. 4. 1σ errors are plotted as solid lines. These incorporate Poisson errors on the counts and the error on the available sky area.

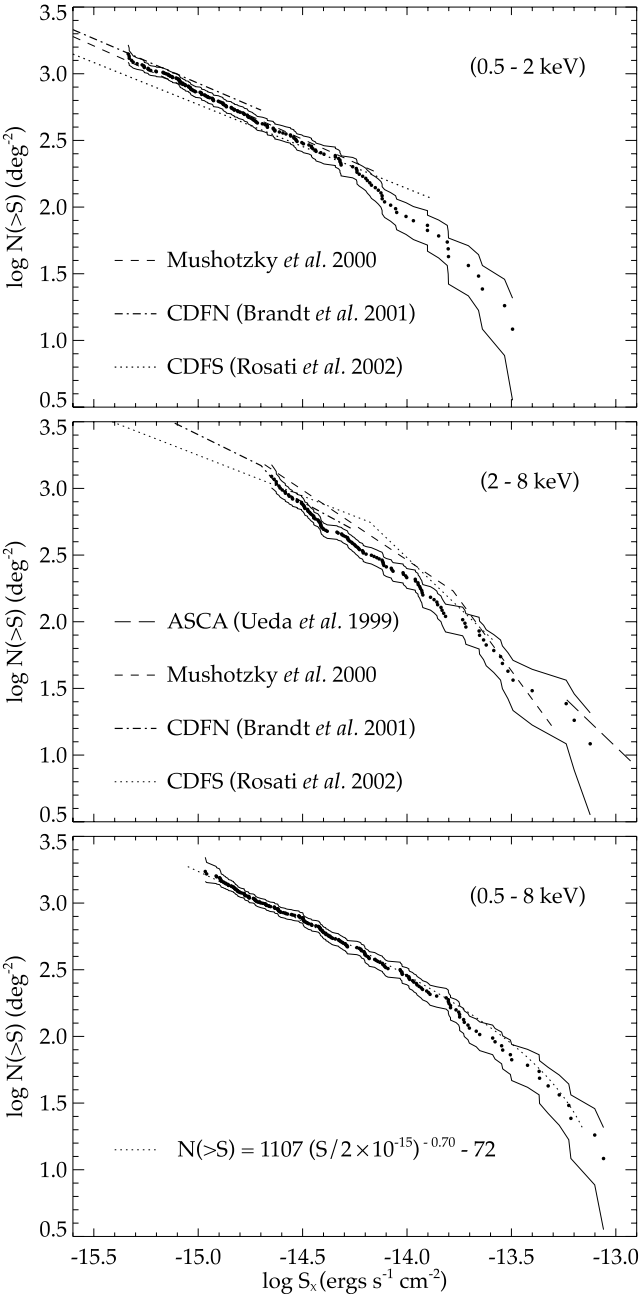

Figure 4. Cumulative number counts per deg^2 for sources detected in the soft-band (top), hard-band (middle) and full-band (bottom) images. Data are plotted as filled circles with solid lines enclosing 1σ errors. Number counts from other recent surveys are estimated from best-fitting power laws quoted in the above references. The full-band plot includes the best-fitting line to the differential counts for sources with $S < 10^{-13}$ erg s^{-1} cm^{-2}.

The limiting flux levels are 1.1×10^{-15}, 4.6×10^{-16} and 2.2×10^{-15} erg cm^{-2} s^{-1} for 0.5–8, 0.5–2 and 2–8 keV, respectively. Simulations show the detection efficiency to be around 99 per cent (see Section 3.1), while Eddington bias may result in an overestimation of the cumulative number counts by approximately 1 per cent (Manners 2002). These factors work to cancel each other and can safely be neglected.

We compare the number counts with those obtained from the CDFN (Brandt et al. 2001), the CDFS (Rosati et al. 2002), and

those of Mushotzky et al. (2000) – M2000. The number counts in the soft band are in good agreement with CDFN and M2000, differing by less than 1σ at the flux limit, while CDFS counts are ∼25 per cent lower ($\sim 2.5\sigma$). The hard-band counts of all four surveys are in reasonably good agreement at our flux limit. At brighter fluxes the surveys differ by $>2\sigma$, most likely as a result of large-scale structure.

The presence of clustering on these scales is well illustrated by the difference in the number counts observed in N1 and N2 (Fig. 5). There are 30 per cent more sources in N1 than N2 in the full band. In particular, there is an overabundance of brighter sources in N1 at a flux of $(1 - 2) \times 10^{-14}$ erg cm^{-2} s^{-1}. Large-scale structure is evident in the source images (Fig. 1), most noticeably as a dearth of sources in the centre of N2. Similar structure can also be seen in images of the CDFS (Giacconi et al. 2001). An analysis of nine *Chandra* fields by Yang et al. (2003) has shown that such clustering is common in the *Chandra* source population.

A striking feature of the number count relations is the difference in slope between soft- and hard-band counts. Fig. 6 overplots the soft- and hard-band counts normalized to an equivalent full-band flux. Normalization is carried out in order to plot both populations on the same flux scale and does not affect the slope of the number counts. The hard-band sources are assumed to have hard spectra and so are arbitrarily normalized using an alpha of 0. The soft-band sources are arbitrarily normalized assuming a soft spectrum with an alpha of 1. The ratio of hard sources to soft sources is seen to increase dramatically towards fainter fluxes. This can be explained through the mechanism of obscuration, which will act to harden the spectra while reducing the flux observed from X-ray sources.

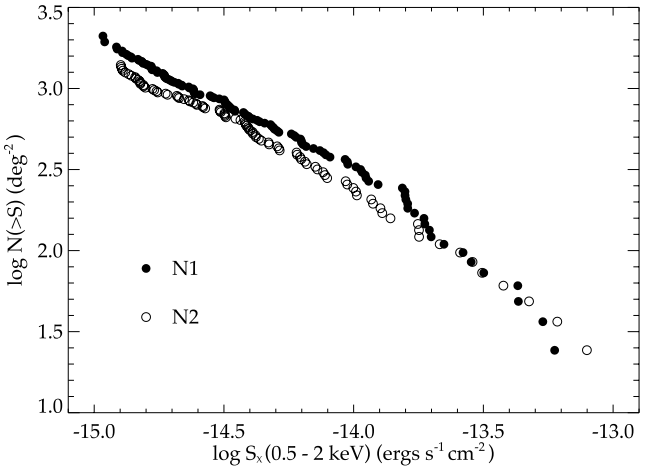

Figure 5. Cumulative source counts (0.5–8 keV band) for the survey fields N1 and N2 are overplotted, illustrating the presence of clustering on scales larger than our field size.

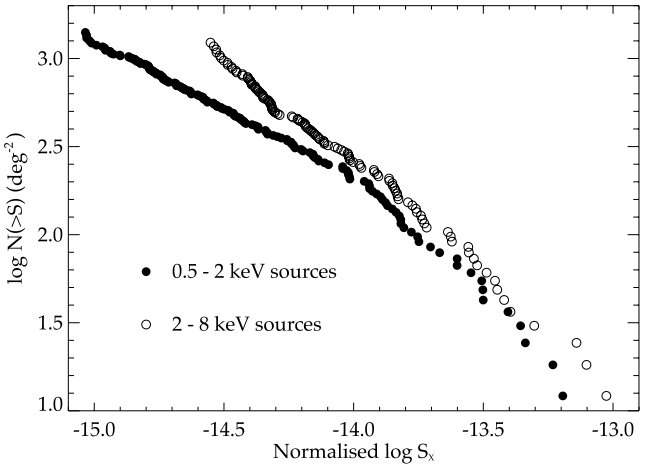

Figure 6. Comparison of the cumulative source counts for the combined fields in the soft and hard bands. The counts have been normalized to an equivalent full-band flux (see text, Section 5.2) to better emphasize the difference in slope between these populations.

Differential number counts per deg^2 per unit flux are plotted in Fig. 7. Error bars display 1σ errors incorporating Poisson errors on the counts and the error on the available sky area. The slope of the differential counts for each band was fitted with a power law using a weighted least-squares fit. A single power law was found to adequately fit the entire flux range for each of the three bands.

For the 0.5–2 keV band over the flux range $(0.57–26) \times 10^{-15}$ erg cm^{-2} s^{-1} we find

$$\log n(S) = (-1.72 \pm 0.09) \log S - (8.0 \pm 1.3). \quad (6)$$

For the 2–8 keV band over the flux range $(2.7–63) \times 10^{-15}$ erg cm^{-2} s^{-1} we find

$$\log n(S) = (-2.07 \pm 0.15) \log S - (12.5 \pm 2.1). \quad (7)$$

For the 0.5–8 keV band over the flux range $(1.4–70) \times 10^{-15}$ erg cm^{-2} s^{-1} we find

$$\log n(S) = (-1.70 \pm 0.08) \log S - (7.4 \pm 1.2). \quad (8)$$

The hard-band differential counts are compared to a maximum likelihood fit from Cowie et al. (2002) to the combined counts from four deep fields (CDFN, CDFS, SSA22 and SSA13). These are found to be in good agreement with the error limits of our survey.

5.3 Contribution to the hard X-ray background

Fig. 8 plots the integrated source flux for our survey (filled circles) for all sources with $S < 10^{-13}$ erg cm^{-2} s^{-1}. At the flux limit of $S_{2-8} = 2.2 \times 10^{-15}$ erg cm^{-2} s^{-1} the resolved flux amounts to 8.5×10^{-12} erg cm^{-2} s^{-1} deg^{-2}. This is equivalent to between 50 and 64 per cent of the 2–8 keV background measured by Vecchi et al. (1999 *Beppo*-Sax) and Ueda et al. (1999 *ASCA*), respectively. To arrive at these values for the total background (as plotted in Fig. 8) the contribution from sources with $S > 10^{-13}$ erg cm^{-2} s^{-1}, as observed by *ASCA* (Della Ceca et al. 1999), has been subtracted. The contribution to the background at fainter fluxes has been extrapolated from the source counts of the CDFN survey (Brandt et al. 2001). By combining the results of our survey with those of the CDFN, the contribution to the background within the flux range 10^{-13}–6×10^{-16} erg cm^{-2} s^{-1} becomes 1.12×10^{-11} erg cm^{-2} s^{-1} deg^{-2}, equivalent to 66 and 84 per cent of the aforementioned backgrounds. To compare the contributions from other surveys, we have used the best fit to the source counts as published by Mushotzky et al. (2000), and Giacconi et al. (2001, 120 ks exposure of the CDFS). These have been normalized at the bright end using the number counts of *ASCA* sources from Della Ceca et al. (1999) to a bright limit of 10^{-13} erg cm^{-2} s^{-1}. The observed discrepancy between the different surveys may be due to the effects of clustering on scales larger than the survey regions.

6 STAR/GALAXY CLASSIFICATION

Deep multicolour optical images have been obtained in both our fields, and will be discussed fully in Paper II. They have identified

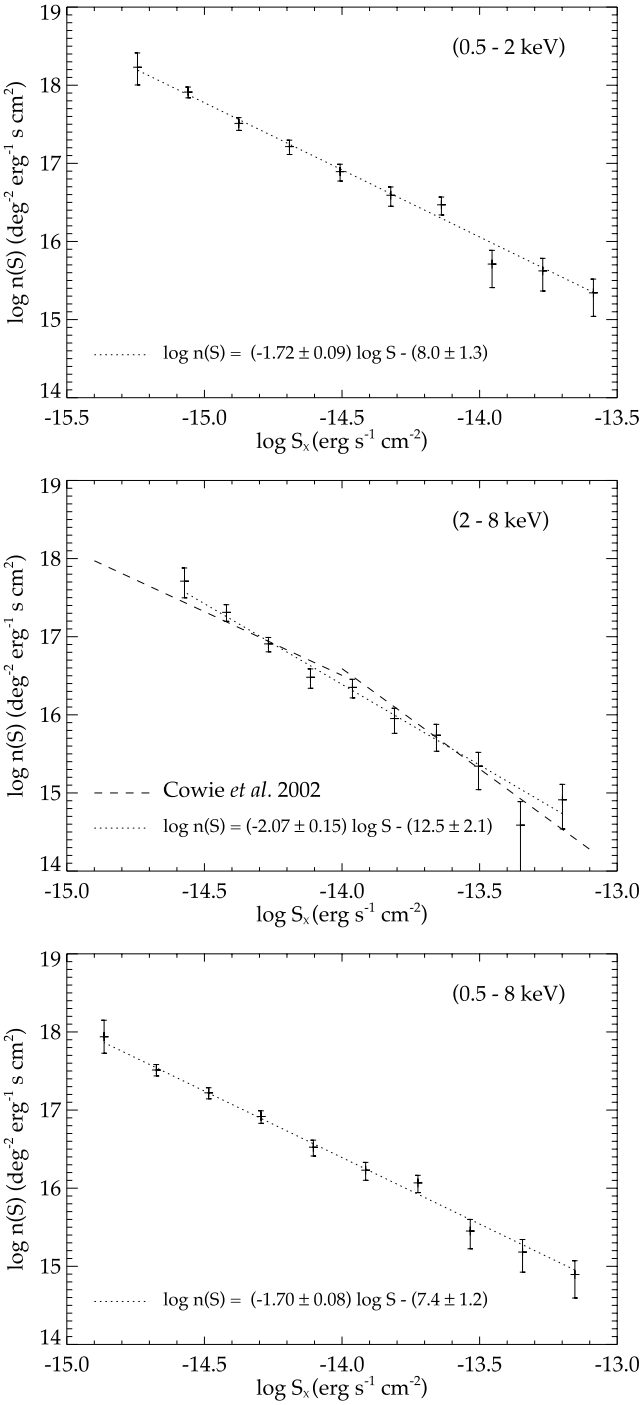

Figure 7. Differential number counts for sources detected in the soft-band (top), hard-band (middle) and full-band (bottom) images. 1σ error bars incorporate Poisson errors on the counts and the error on the available sky area. A weighted least-squares best fit is displayed with 1σ error ranges.

the optical counterparts of our X-ray sources in r'-band images with limiting magnitudes of ∼26. Source optical morphologies are classified according to agreement with a stellar PSF, as quantified in the SExtractor 'stellarity' parameter, CLASS STAR (Bertin & Arnouts 1996). The output of a neural network classifier, the value of this parameter ranges from 0.0 for significantly extended sources to 1.0 for those with perfectly stellar PSFs. For our *Chandra* sample, we divide sources with quasar-like and galaxy-like counterparts at CLASS STAR 0.8. In practice, morphological classification is increasingly ambiguous for fainter sources with lower S/N and cannot be considered reliable near to the image limiting magnitude. A number of X-ray sources remain unclassified where they are associated with blank fields, gaps in the data, or are near to bright contaminating sources in the optical images.

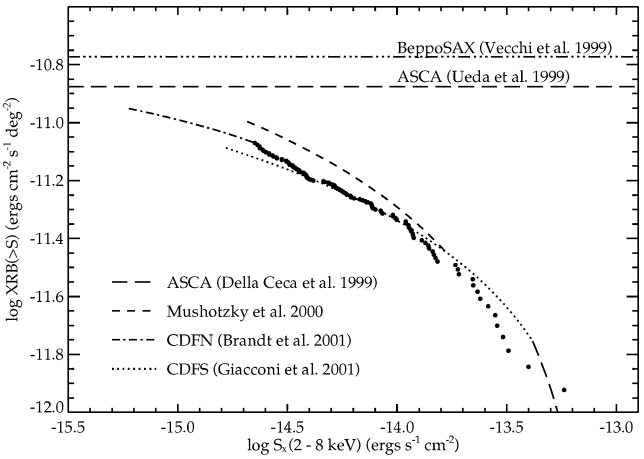

Figure 8. Contribution to the hard X-ray background. The integrated hard-band fluxes for sources fainter than 1×10^{-13} erg cm^{-2} s^{-1} in this survey are plotted as filled circles. The contributions from other surveys are extrapolated from reported number count slopes. Plotted values for the total background exclude sources brighter than 1×10^{-13} erg cm^{-2} s^{-1}.

The cumulative soft-band source counts for each group have been calculated and are plotted in Fig. 9. At bright X-ray fluxes quasar-like sources are the most numerous. However, their number counts flatten appreciably below a flux of $\sim 5 \times 10^{-15}$ erg cm^{-2} s^{-1}. At fainter fluxes the fraction of galaxy-like sources dramatically increases. At the flux limit of 4.6×10^{-16} erg cm^{-2} s^{-1} there are 35 per cent more galaxy-like sources than quasar-like sources.

An X-ray luminosity function (XLF) from Boyle et al. (1994), invoking pure luminosity evolution, was used to obtain number count predictions for broad-line AGN. This was based on observations of 107 quasi-stellar objects (QSOs) from a deep *ROSAT* survey. These QSOs reached a flux limit of $\sim 5 \times 10^{-15}$ erg cm^{-2} s^{-1} in

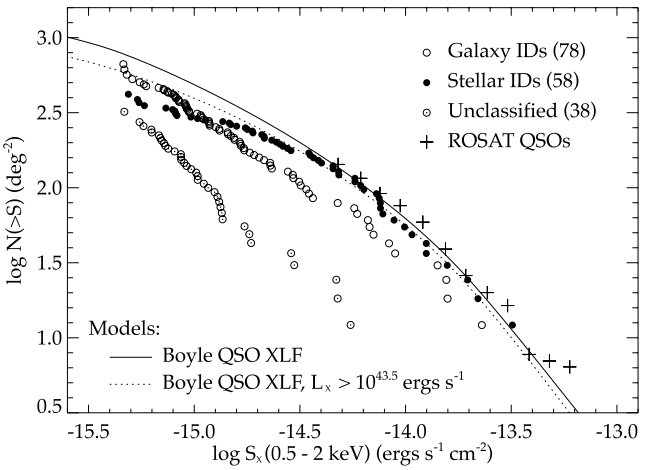

Figure 9. Soft-band number counts split between quasar-like, galaxy-like and unclassified (blank fields, etc.) optical counterparts. In comparison, the QSOs observed with *ROSAT* (Boyle et al. 1994) and associated models for the QSO X-ray luminosity function are overplotted.

the 0.5–2 keV band. We use their best-fitting model (model S), with an exponential decline in the quasar population beyond $z = 2.7$, to construct a prediction for the soft-band QSO number counts. This is overplotted in Fig. 9 (solid line) to compare with the cumulative number counts for sources with quasar-like optical IDs. The Boyle XLF also includes relatively low luminosity AGN which may possibly be resolved into galaxies in our r'-band images. A second model has therefore been added which excludes AGN with a 0.5–2 keV luminosity less than $10^{43.5}$ erg s^{-1} (dotted line).

The models are well matched to the data up to the flux limit of the *ROSAT* survey. However, beyond this they overpredict the number of quasar-like sources. In the limiting case where all the unclassified sources are stellar, the data become a good fit to the first model. In the more likely outcome that most of the unclassified objects are galaxies, the data may still be a reasonable fit to the Boyle XLF as long as a luminosity cut-off is applied.

In Fig. 10 we plot full-band X-ray flux versus r'-band magnitude for our *Chandra* sources; compare with figure 3 of Barger et al. (2002), figure 16 of Giacconi et al. (2002), figure 6 of Mainieri et al. (2002). In this figure, as in those in Section 7, we indicate source morphology only for sources with $r' < 24$, which have unambiguous classifications. Overplotted are lines of constant X-ray to optical ratio, appropriate for the Sloan Gunn r' filter:

$$\log\left(\frac{f_X}{f_{r'}}\right) = \log f_X + 5.67 + \frac{r'}{2.5}. \quad (9)$$

Among point-like sources optical luminosity is seen to scale with X-ray luminosity; nearly all exhibit X-ray to optical ratios, f_X/fr', of 0.1 to 10. In contrast, sources with galaxy-like morphology show no tight relation between X-ray and optical fluxes, suggesting that the host galaxies and not the central AGN dominate the optical emission. Four spectroscopically confirmed Type II AGN (discussed fully in Willott et al. 2003 and Perez-Fournon et al., in preparation) are marked in Fig. 10, only one of which has a notably high value of f_X/fr'. Of the six point-like sources with $f_X/fr' < 0.1$, three are spectroscopically confirmed stars, as noted in the figure.

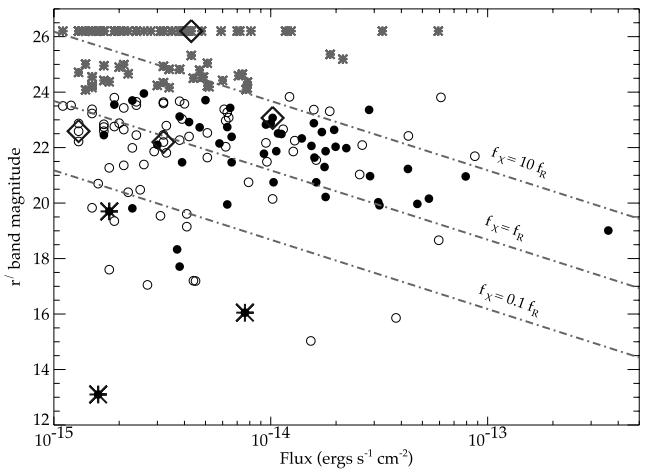

Figure 10. X-ray flux versus r'-band magnitude for *Chandra* sources. Symbols denote sources with galaxy-like morphology (open circles), point-like morphology (closed circles), and ambiguous morphology (small stars), as well as spectroscopically confirmed stars (large stars) and spectroscopically confirmed Type II AGN (diamonds).

7 HARDNESS RATIOS

Broad-band X-ray hardness ratios (HRs) were calculated for each source, and were defined as

$$HR = \frac{(H - S)}{(H + S)},$$

where H and S are the background-subtracted source counts in the hard (2.0–8.0 keV) and soft (0.5–2.0 keV) bands, respectively. Net source counts were extracted from the exposure corrected hard- and soft-band images within circular regions centred on the WAVDETECT positions. The apertures were scaled to mimic the degradation of the *Chandra* PSF with off-axis angle in each band, and had minimum radii of 10 pixels. Background counts were extracted from source-free images in annuli around each source, and subtracted. The net, source and background counts thus obtained were consistent within the errors to those reported by WAVDETECT. We find that background subtraction and exposure correction of the source counts have increasingly significant effects on the derived HRs toward fainter fluxes.

Hardness ratios are plotted against full-band X-ray flux in Fig. 11. As noted by earlier surveys (Mushotzky et al. 2000; Giacconi et al. 2001; Hasinger et al. 2001; Hornschemeier et al. 2001), harder sources are seen at fainter fluxes, signalling the emergence of the population comprising the majority of the X-ray background (XRB). Assuming $\alpha = 0.7$ power-law spectra typical of AGN, the range of hardnesses observed suggests absorbing columns of up to $N_{\rm H} \sim 10^{23}$ at zero redshift. As apparent absorption column scales as $(1 + z)^{2.6}$ (see, for example, Barger et al. 2002), actual columns in higher redshift sources will be significantly higher. The range of observed columns is consistent with that seen in other deep surveys (e.g. Barger et al. 2002; Mainieri et al. 2002) in which growing samples of spectroscopic identifications have so far revealed only a handful of more heavily obscured objects.

The symbols in Fig. 11 refer to the morphological classification discussed in Section 5.2. We see that the point-like sources generally cluster around a HR of −0.5 at all fluxes. This value is consistent with a power law of $\alpha \simeq 0.7$ modified only by Galactic absorption, and is typical of Type I QSOs. Sources with

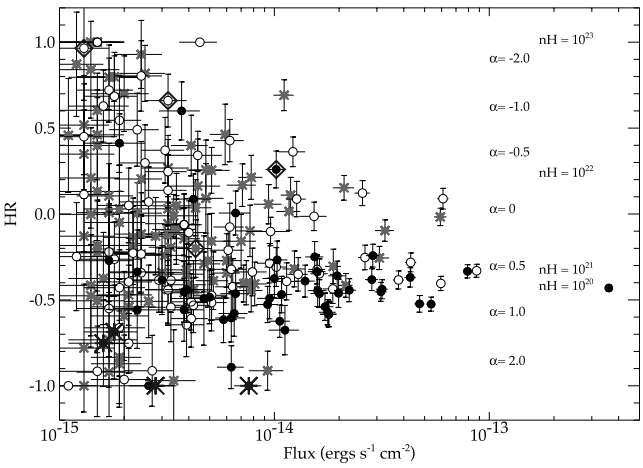

Figure 11. Full-band X-ray flux versus HR for *Chandra* sources, with symbols as in Fig. 10: filled circles, QSOs; open circles, galaxies; crosses, unclassified sources. The values indicated on the right are the expected HR of absorbed power-law spectra at $z = 0$, with various energy indices assuming galactic absorption, and with various absorbing columns assuming an unabsorbed power law of $\alpha = 0.7$.

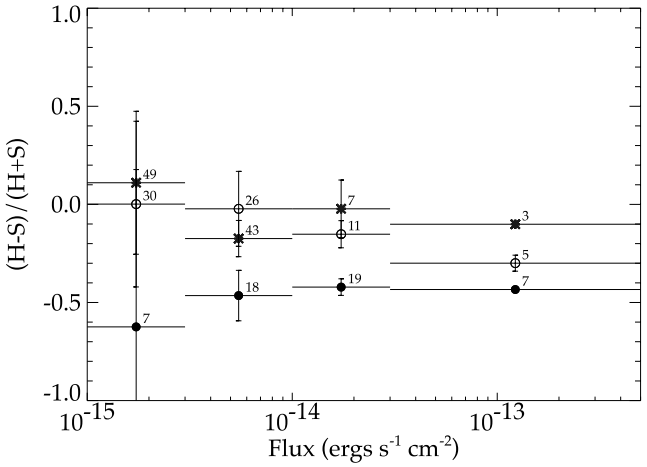

Figure 12. Error-weighted average HR for sources of different morphology binned by flux, with symbols as in Fig. 11. The number of sources in each bin are indicated, and the error bars indicate the variance within the bin.

galaxy-like morphology are seen in this region, but also populate increasingly hard regions of the diagram at fainter fluxes. Three of the four confirmed Type II AGN are conspicuously hard. The trend to harder X-ray spectra at fainter X-ray fluxes for optically extended sources is more clearly seen in Fig. 12, which shows error-weighted average HRs for sources of different morphologies binned by flux.

8 EXTENDED SOURCES

To search for X-ray sources on scales much larger than the PSF we have run the source detection algorithm WAVDETECT using wavelet scales of 16, $16\sqrt{2}$, 32, $32\sqrt{2}$, and 64 pixels (see Section 3). Any sources found in addition to those already detected were checked by inspecting the adaptively smoothed *Chandra* images.

No additional sources were detected in N1 and inspection of the smoothed image reveals no hint of large extended sources. In N2 there are two significant extended sources. This is equivalent to $\sim$12 deg^{-2} over the two fields at a limiting soft-band flux of $\sim 5 \times 10^{-15}$ erg s^{-1} cm^{-2}. This source density is consistent with the number counts reported by Bauer et al. (2002) and references therein (their figure 6).

The most significant of the two detected sources is CXOEN2 J163637.3+410804 displayed in Fig. 13. The X-ray position (centred on the brightest component of the extended source) is at J2000 16:36:37.38+41:08:04.9. There are 207 net source counts in the 0.5–2 keV band in an area corresponding to a factor of 17.5 larger than the PSF. This extrapolates to a soft-band flux of $1.46 \pm 0.15 \times 10^{-14}$ erg cm^{-2} s^{-1}, although this includes the flux from point source N2_101 (CXOEN2 J163633.8+410730) which lies within the extended source region at a distance of 52 arcsec from the core. The r'-band image of this region reveals the presence of a galaxy cluster.

Spectra of three cluster members show absorption features consistent with a redshift of 0.4232 (Perez-Fournon et al., in preparation). The ACIS-S pulse height spectrum of the cluster (Fig. 14) and appropriately weighted response matrices were extracted using standard CIAO tools, and spectral analysis was performed using XSPEC. The data are well fitted with a Raymond–Smith emission model for hot, diffuse gas with an abundance of 0.3 solar and a plasma temperature of 2.73 ± 0.81 keV.

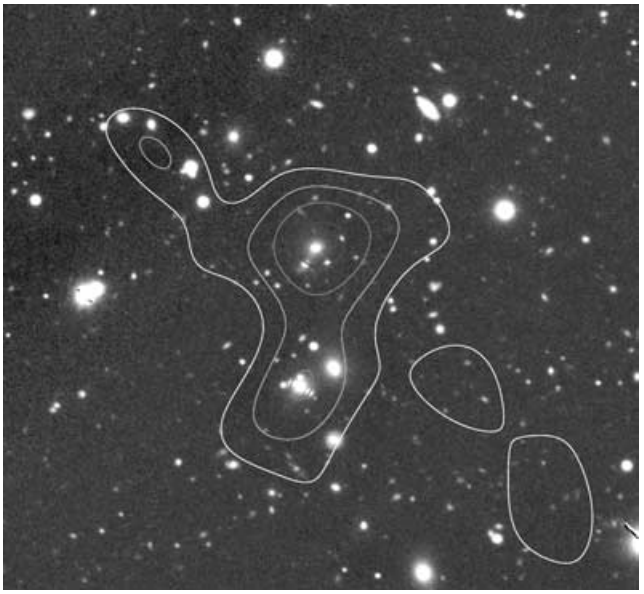

Figure 13. This 2.5 × 2.5 arcmin^2 r'-band image displays a cluster of galaxies which coincides with the extended X-ray source CXOEN2 J163637.3+410804. The X-ray contours have been obtained by smoothing the *Chandra* data with a Gaussian of 10 arcsec. The X-ray position is centred on the brightest component of the extended source. This figure can be seen in colour in the on-line version of the journal in *Synergy*.

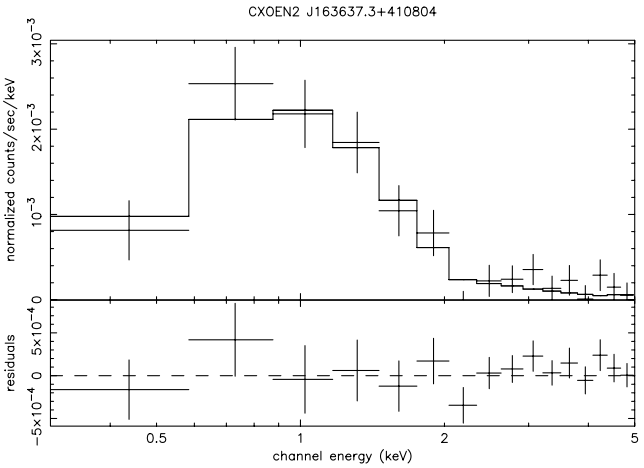

Figure 14. ACIS-S pulse height spectrum of CXOEN2 J163637.3+410804. The model is a Raymond–Smith emission spectrum at the cluster redshift with 0.3 solar abundance, and yields a best-fitting plasma temperature of 2.73 keV.

The second extended X-ray source in N2 is also associated with a galaxy cluster. This source (shown in Fig. 15) is at the very edge of the *Chandra* image. Its position is approximately J2000 16:37:28.5+41:00:13, although the centroid may in fact lie outside the area of the image. For this reason, the identification and properties of this source will not be reported here.

9 CONCLUSIONS

We have presented the *Chandra* source catalogues for deep (75 ks) observations of the ELAIS fields N1 and N2. A total of 233 X-ray point sources are detected: 225 in the 0.5–8 keV band, 182 in the

Figure 15. This 3×3 arcmin^2 r'-band image displays a cluster of galaxies which coincides with an extended X-ray source very close to the edge of the N2 *Chandra* image. The X-ray contours have been obtained from an adaptively smoothed *Chandra* image and can only be used as an illustration due to edge effects. The centroid of the X-ray source is at approximately J2000 16:37:28.5+41:00:13. This figure can be seen in colour in the on-line version of the journal in *Synergy*.

0.5–2 keV band, and 124 in the 2–8 keV band. In addition, two extended sources are detected in N2 in the 0.5–2 keV band and are found to be associated with galaxy clusters.

An overdensity of sources is found in N1 with 30 per cent more sources than N2. This difference is present in both the soft- and hard-band number counts and may be attributed to large-scale structure. A similar variance is seen between other deep *Chandra* surveys.

Source count statistics reveal an increasing fraction of hard sources at fainter fluxes. The number of galaxy-like counterparts also increases dramatically towards fainter fluxes, consistent with the emergence of a large population of obscured sources. Additionally, objects with galaxy-like and faint optical counterparts exhibit harder X-ray spectra towards fainter fluxes, consistent with significant absorbing columns in this population.

The source catalogues and further information regarding the ELAIS deep X-ray survey can be found at http://www.roe.ac.uk/∼jcm/edxs.

ACKNOWLEDGMENTS

JM acknowledges the support of a PPARC Studentship and would like to thank the Institute for Astronomy (IfA), Edinburgh for providing extra funds for the completion of this paper.

REFERENCES

Almaini O., Shanks T., Boyle B. J., Griffiths R. E., Roche N., Stewart G. C., Georgantopoulos I., 1996, MNRAS, 282, 295
Almaini O. et al., 2003, MNRAS, 338, 303
Barger A. J., Cowie L. L., Mushotzky R. F., Richards E. A., 2001a, AJ, 121, 662
Barger A. J., Cowie L. L., Steffen A. T., Hornschemeier A. E., Brandt W. N., Garmire G. P., 2001b, ApJ, 560, L23
Barger A. J., Cowie L. L., Brandt W. N., Capak P., Garmire G. P., Hornschmeier A. E., Steffen A. T., Wehner E. H., 2002, AJ, 124, 1839
Barger A. J., Cowie L. L., Capak P., Alexander D. M., Bauer F. E., Brandt W. N., Garmire G. P., Hornschmeier A. E., 2003, ApJ, 584, L61
Bauer F. E. et al., 2002, AJ, 123, 1163
Bertin E., Arnouts S., 1996, A&AS, 117, 393
Boyle B. J., Griffiths R. E., Shanks T., Stewart G. C., Georgantopoulos I., 1994, MNRAS, 271, 639
Brandt W. N. et al., 2001, AJ, 122, 2810
Ciliegi P. et al., 1999, MNRAS, 302, 222
Cowie L. L., Garmire G. P., Bautz M. W., Barger A. J., Brandt W. N., Hornschemeier A. E., 2002, ApJ, 566, 5
Della Ceca R., Castelli G., Braito V., Cagnoni I., Maccacaro T., 1999, ApJ, 524, 674
Fox M. J. et al., 2002, MNRAS, 331, 839
Freeman P. E., Kashyap V., Rosner R., Lamb D. Q., 2002, ApJS, 138, 185
Gehrels N., 1986, ApJ, 303, 336
Giacconi R. et al., 2001, ApJ, 551, 624
Giacconi R. et al., 2002, ApJS, 139, 369
Hasinger G., Burg R., Giacconi R., Hartner G., Schmidt M., Trümper J., Zamorani G., 1993, A&A, 275, 1
Hasinger G., Burg R., Giacconi R., Schmidt M., Trumper J., Zamorani G., 1998, A&A, 329, 482
Hasinger G. et al., 2001, A&A, 365, L45
Hornschemeier A. E. et al., 2001, ApJ, 554, 742
Ivison R. J. et al., 2002, MNRAS, 337, 11
Mainieri V., Bergeron J., Hasinger G., Lehmann I., Rosati P., Schmidt M., Szokoly G., Della Ceca R., 2002, A&A, 393, 425
Maiolino R., Marconi A., Salvati M., Risaliti G., Severgnini P., Oliva E., La Franca F., Vanzi L., 2001, A&A, 365, 28
Manners J. C., 2002, PhD thesis, Univ. Edinburgh
Mushotzky R. F., Cowie L. L., Barger A. J., Arnaud K. A., 2000, Nat, 404, 459
Oliver S. J. et al., 2000, MNRAS, 316, 749
Rosati P. et al., 2002, ApJ, 566, 667
Scott S. E. et al., 2002, MNRAS, 331, 817
Tozzi P. et al., 2001, ApJ, 562, 42
Ueda Y. et al., 1999, ApJ, 518, 656
Vecchi A., Molendi S., Guainazzi M., Fiore F., Parmer A. N., 1999, A&A, 349, L73
Willott C. J. et al., 2003, MNRAS, 339, 397
Yang Y., Mushotzky R. F., Barger A. J., Cowie L. L., Sanders D. B., Steffen A. T., 2003, ApJ, 585, 85

This paper has been typeset from a TEX/LATEX file prepared by the author.